Nonlinear Dyn (2007) 49:163–191
DOI 10.1007/s11071-006-9120-2

ORIGINAL ARTICLE

Numerical stability analysis and control of umbilical–ROV systems in one-degree-of-freedom taut–slack condition

Mario Alberto Jordán · Jorge Luis Bustamante

Received: 9 February 2005 / Accepted: 21 June 2006 / Published online: 12 October 2006

Abstract In this paper, the stability of an umbilical–ROV system under nonlinear oscillations in heave motion is analyzed using numerical methods for the uncontrolled and controlled cases comparatively. Mainly the appearance of the so-called taut–slack phenomenon on the umbilical cable produced by interactions of monochromatic waves and an operated ROV is specially focused. Nonlinear elements were considered as nonlinear drag damping, bilinear restoring force and saturation of the actuators. Free-of-taut/slack stability regions are investigated in a space of physical bifurcation parameters involving a set of both operation and design parameters. They indicate a wide diversity in qualitative behaviors, both in the periodicity and possible routes to chaos from the stability regions to outside. For detection of periodicity of the nonlinear oscillations inside and outside the stability regions, a method based on Cauchy series is developed. The first part of the results is dedicated to the stability of the uncontrolled dynamics. These results suggest the design of a control system that is able to counteract hefty hauls of the cable during the sinking/lifting operation under perturbation. A combination of a force and cinematic controller based on nonlinear model–reference control is proposed. Through a comparative study of the stability regions for uncontrolled and controlled dynamics, it is shown that the control system can extend considerably these regions without appearance of the taut–slack phenomenon despite the presence of wave perturbations. The limits between the taut and taut–slack zones are defined by the wave steepness and the available energy of the actuators.

Keywords Cauchy series · Chaos · Drag coefficient · Force control · Nonlinear hydrodynamics · Nonlinear stiffness · ROV dynamics · Stability regions · Taut–slack phenomenon · Cinematic control

1 Introduction

Tethered subsea units such as remote operated underwater vehicles (ROVs) are widely used in offshore engineering, scientific investigations, and rescue operations [6, 8, 16]. Due to the inherent nonlinear equations of motions, ROVs require the design of sophisticated controllers that involve automatic speed control, systems for dynamic positioning and tracking, as well as autopilot systems for automatic steering of depth and altitude (for basic details, see [8]).

Also, the dynamics of the umbilical cable interacts with the body and the environment in a complex way, mainly at low and middle levels of depths, where waves and currents are strong. The top end of the cable is generally subject to motions of the supporting vessel – usually a surface ship – which, in turn, responds to

M. A. Jordán (✉) · J. L. Bustamante
Departamento de Ingeniería Eléctrica y de Computadoras, Universidad Nacional del Sur, Av. Alem 1253-8000, Bahía Blanca, Argentina
e-mail: mjordan@criba.edu.ar

the sea excitation. Additionally, strong currents may act directly along the cable and cause strumming oscillations due to vortex shedding phenomena. The main effect on the vehicle is that its forward speed is reduced and undesirable rotational motions are induced [4].

Even when vortex shedding in cables could be not so important [11], a taut–slack phenomenon of the umbilical cable may be significant when a combination of forces due to strong currents or thrusters and superficial waves produces acceleration in the port/starboard direction up to the advent of intermittent slackness and hauls. Afterwards, eventually, there may occur a lack of motion predictability, making it difficult for the operator to take control actions. Commonly, high frequency and hefty oscillations of the cable are involved in these transitions.

Also, this effect may occur in a more simple situation, e.g., in the sinking of the unit up to or lifting from a working depth. These are usually subject to resonance phenomena mainly due to time-varying lengths of the cable which changes the natural frequency of the system [2, 9, 10, 19]. If the unit is deployed in a sea with weak currents, the dynamics can be simplified to a simple heave motion alone. In such situation, the rate at which the cable varies its length can affect the dynamics of the cable–body system, manifesting quite qualitatively different behaviors [13, 18].

A special aspect of the operation is that the cable tension can become null if the ascent of the ROV occurs sufficiently fast. This can also arise for relatively large frequencies of the wave. Huang [9] analyzed the dynamics of a cable–body system under taut–slack conditions using a piecewise linear equation of the cable force. Herein, the cable stiffness is assumed to have linear elastic traction and null compression, while the damping is considered constant and the body with punctual geometry (cf. [21]). Using a dimensionless differential equation and considering an harmonic motion of the upper cable extreme, the system behavior is shown to manifest nonlinear oscillations.

The simplified model of Huang, however, does not cover the nonlinear effects of damping and added mass. Hydrodynamic aspects may influence the qualitative response of the ROV decisively [7, 17]. For instance, the body can radiate and hydrodynamics memory effects can influence the damping and the inertia at lesser depths. Another point which is not considered in the Huang's model is the nonlinear drag term in the equation of the forced oscillator, which depends on the body shape and Reynolds number.

In order to simplify our analysis of stability and controller design, we examine simple spheric forms of the ROV with different diameters providing varying drag resistance and inertia forces. In our contribution, we aim to provide a more realistic stability study of a ROV motion under taut–slack phenomenon in the heave motion through simulations and numeric stability analysis. The fidelity of the results in the simulations will be backed up by the accuracy of the physical laws that describe the dynamics more rigorously than previous models.

Since an analytic solution does not exist for the nonlinear equations of motion, we propose numeric methods for searching bifurcations of stable solutions based on temporal series analysis extracted from Poincaré maps. Regions that characterize stability are also constructed in a space of different bifurcation parameters, namely cable length and stiffness, wave amplitude and frequency, wet area of the ROV, and magnitudes of thruster forces. Fundamental information about the dynamic behavior of the umbilical–ROV system in taut–slack condition and vertical operation can be obtained from them in physical models with different degrees of knowledge.

A second aim in this paper includes designing a control system for the sinking/lifting process. Nonlinearities that unfavorably affect the performance of the control will be compensated by nonlinear feedback. The main control objective will be focused on rejecting eventual taut–slack behaviors, employing thrusters for the purpose of vertical displacements and adjustments in the velocity of the hoisting crane motor unit. Another control objective will be looked at the control of the cable tension in order to get it away from critical values. A basis for the control system analysis will be stability regions for a set of bifurcation parameters. In the paper, numerous simulations have been given to illustrate the features of the control system in comparison with the former uncontrolled umbilical–ROV system.

2 Dynamics

Let us consider the following scenario for our study. During the sinking/lifting operation of a ROV, harmonic vertical motion of the hoisting crane due to the action of a monochromatic wave causes taut–slack

transitions in the umbilical cord. Usually, the ROV is being deployed over the aft of the ship. The cable remains on a vertical plane and takes a particular bent shape given by the action of a current as shown in Fig. 1. Depending on the ROV operation and the crane jib elevation, the wire can be tensed from both upper and lower extremes (taut condition). Also, when both extremes move in opposite direction, a looseness of the wire can take place (slack condition). This particular motion occurs intermittently, mainly when a periodic excitation like a wave acts on the system.

In this paper, we analyze the phenomenon in 1 degree of freedom namely vertically, as for example in the sinking/lifting phase and assume that there exists a static equilibrium tension of the cable given by the weight of the vehicle in water (see Fig. 2). Additionally, we describe the nonlinear hydrodynamics completely in order to show that complex behaviors can happen from this simple operation with monochromatic excitation.

For the analysis of the dynamics of the umbilical–ROV system, following general assumptions are considered:

(a) motion takes place vertically (heave mode),
(b) mass cable is inappreciable,
(c) ROV has a slight positive buoyancy and its hull is spherical,
(d) mass of the surface ship is very large in comparison with ROV mass,
(e) cable has a null stiffness in slack condition,
(f) sea provides a persistent monochromatic vertical excitation of the pivot at which cable is attached,
(g) ROV thrusters for vertical push and hoisting crane motor unit are available for control purposes.

The position of the ROV in the sinking/lifting operation is appropriately given by the immersion depth d with respect to the water line. When the quantity $b - a \sin \omega t$ increases for the top end of the cable and the quantity d (cf. Fig. 2) decreases for the bottom end,

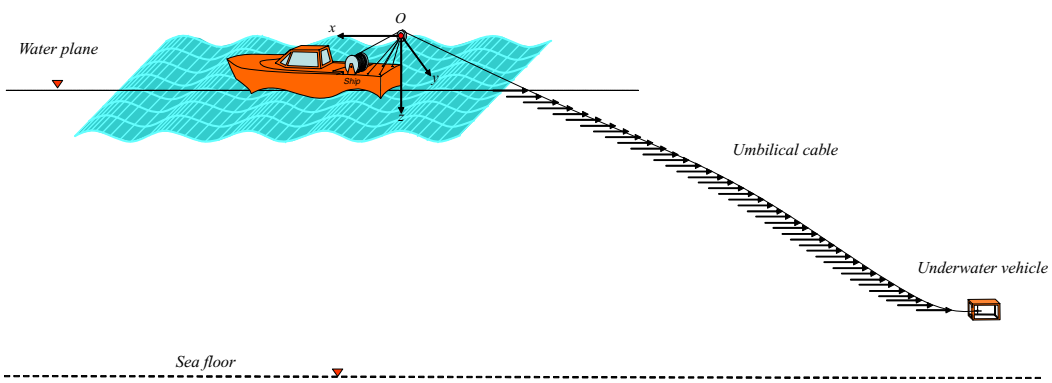

Fig. 1 Remotely operated vehicle and surface ship

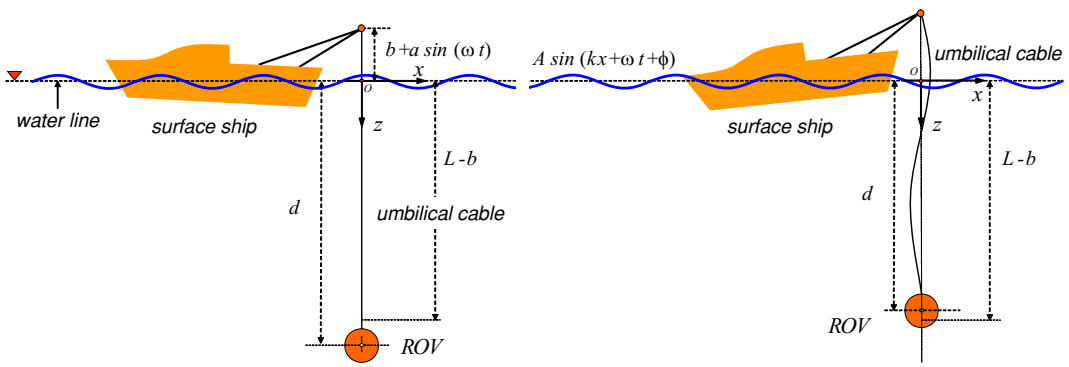

Fig. 2 Umbilical–ROV system in taut condition (left) and slack condition (right)

the tension of the cable is

$$F_c = \frac{E A_0}{L}(d - L + b - a\sin(\omega t)), \tag{1}$$

where L is the length of the cable, b the crane jib elevation, $a\sin(\omega t)$ the oscillation about it due to a monochromatic wave, E the Young's modulus of the cable, and A_0 its cross section. On the other side, the cable remains loose when $F_c = 0$.

These cable conditions are summarized as

$$d - L + b - a\sin(\omega t) > 0 \rightarrow \text{taut condition } F_c > 0 \tag{2}$$

$$d - L + b - a\sin(\omega t) \leq 0 \rightarrow \text{slack condition } F_c = 0. \tag{3}$$

From (1)–(3), it is evident that the characteristic stress–deformation is continuous but broken at $d - L + b = a\sin(\omega t)$, i.e., in the transition from slack to taut states and vice versa. Besides, the cable stiffness $(E A_0)/L$ is inversely proportional to L.

For characterizing the heave motion, a single-degree-of-freedom model is applied. The dynamics is approximated by different mathematical approaches, each one involving a progressive increment of physical knowledge, starting from a coarse characterization with a simple model of the hydrodynamics up to a more refined model including a velocity-depending drag coefficient and radiation-potential forces. Each of these descriptions is analyzed separately and then comparatively under the same setting of common parameters.

2.1 Equations of motion: Model 1

The equations of motion in vertical z-axis are subject to the rigid body mechanics and the hydrodynamics given by Potential Flow Theory and Morison's law.

Let the hydrodynamics of the umbilical–ROV system be uniquely described by the so-called added mass of the ROV geometry and the drag force with a constant drag coefficient.

The parameters of the system are the ROV mass m, the so-called added mass m_∞ due to acceleration of the water particles in the surrounding of the ROV surface, the gravity acceleration g, the sea water density ρ, the hydrodynamic drag force coefficient C_D, the diameter of the ROV D, and finally the resultant of the vertical thruster force F_t.

As the cable characteristic has two linear portions according to (2) and (3), the equations can be established separately for these two states. On the one hand, the following is valid for the taut condition (2)

$$(m + m_\infty)\ddot{d} + \frac{\pi\rho D^2}{8}C_D\,\dot{d}|\dot{d}| + \frac{E A_0}{L}(d - L + b) + \frac{\pi\rho D^3}{6}g + F_t = mg + \frac{E A_0 a}{L}\sin(\omega t), \tag{4}$$

and, on the other hand, the following is accomplished for the slack condition (3)

$$(m + m_\infty)\ddot{d} + \frac{\pi\rho D^2}{8}C_D\,\dot{d}|\dot{d}| + \frac{\pi\rho D^3}{6}g + F_t = mg. \tag{5}$$

Then, a solution $d(t)$ can be composed piecewise from the solutions of (4) and (5).

The approximation of the hydrodynamics through the constant coefficient m_∞ is sufficiently accurate for large depths. Practically, this is fulfilled for $d \gg D$. For the spherical surface considered, the added mass is equal to the half of the fluid displaced by the mass of the body, i.e., $m_\infty = (\rho\pi D^3)/12$. In the case study, as the ROV is assumed with a slightly positive buoyancy, it is valid $(m)/(m_\infty) \gtrapprox 2$.

2.2 Equations of motion: Model 2

In addition to the added mass for the ROV geometry, we can incorporate a velocity-dependent drag coefficient for the same spherical geometry (see Figs. 3 and 4). This leads to a better description of the system dynamics.

It is worth noticing that C_D depends basically on the shape of the ROV along the motion direction and will be consequently classified as a design parameter. However, as it depends also on Reynolds number, which changes during operation, it is also an operation parameter. The Reynolds number is defined as

$$Re = \frac{\rho D}{\eta_{H_2O}}\dot{d} = 1.026 \times 10^6 D\,\dot{d} \tag{6}$$

where $\rho = 1.026 \times 10^3\ \text{kg/m}^3$ is the density of sea water and $\eta_{H_2O} = 10^{-3}\ \text{kg/ms}$ the dynamic viscosity of

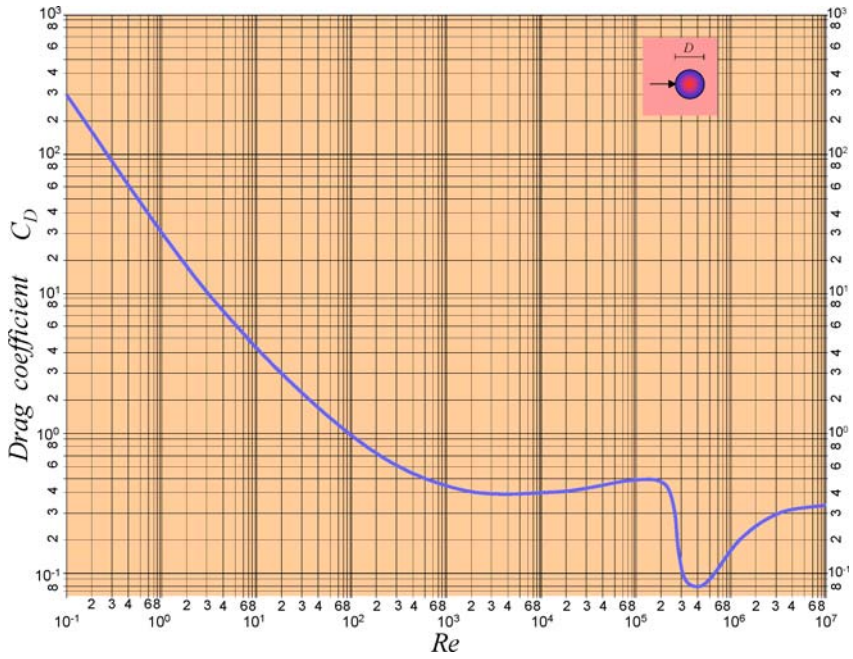

Fig. 3 Drag coefficient for a spherical-shape body as function of Reynolds number

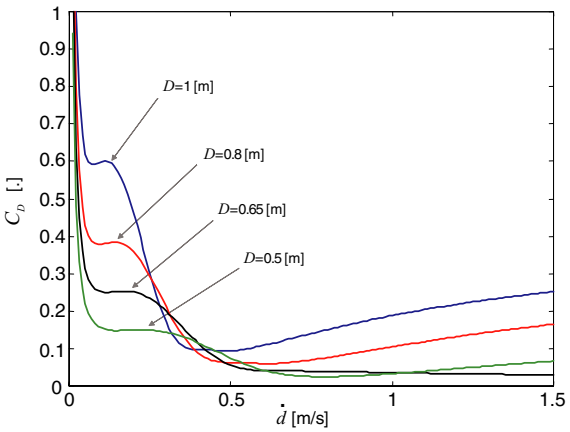

Fig. 4 Drag coefficients as function of the ROV velocity for different diameters

water. Taking into account Fig. 3, C_{D} can be approximately calculated in the range $Re \in [10^{-1}, 10^{7}]$ by means of a linear regression like

$$C_{\mathrm{D}} = \varphi_{Re}^{T}\theta_{Re}, \tag{7}$$

with

$$\varphi_{Re}^{T} = [(\log_{10} Re)^{21}, (\log_{10} Re)^{20}, \ldots, (\log_{10} Re)^{2}, (\log_{10} Re), 1] \tag{8}$$

$$\begin{aligned}\theta_{Re} = [&-8.332 \times 10^{-9}, 5.389 \times 10^{-7}, -1.592 \times 10^{-5}, 2.841 \times 10^{-4}, -3.412 \times 10^{-3},\\ &2.905 \times 10^{-2}, -1.798 \times 10^{-1}, 8.132 \times 10^{-1},\\ &-2.648, 5.925, -7.871, 2.121, 12.407,\\ &-20.641, 6.411, 17.352, -26.194, 28.856,\\ &-45.340, 62.735, -56.695, 27.193]^{T}\end{aligned}$$

Based on experimental data in steady state, Equation (7) describes a polynomial approximation of degree 21 of the curve in Fig. 3.

In the new model, equations of motion are given first for the taut condition (2) as

$$(m + m_{\infty})\ddot{d} + \frac{\pi\rho D^2}{8} C_{\mathrm{D}}(\dot{d})\,\dot{d}|\dot{d}| + \frac{E A_0}{L}(d - L + b) + \frac{\pi\rho D^3}{6} g + F_{\mathrm{t}} = mg + \frac{E A_0 a}{L}\sin(\omega t), \tag{9}$$

and then for slack condition (3)

$$(m + m_{\infty})\ddot{d} + \frac{\pi\rho D^2}{8} C_{\mathrm{D}}(\dot{d})\,\dot{d}|\dot{d}| + \frac{\pi\rho D^3}{6} g + F_{\mathrm{t}} = mg. \tag{10}$$

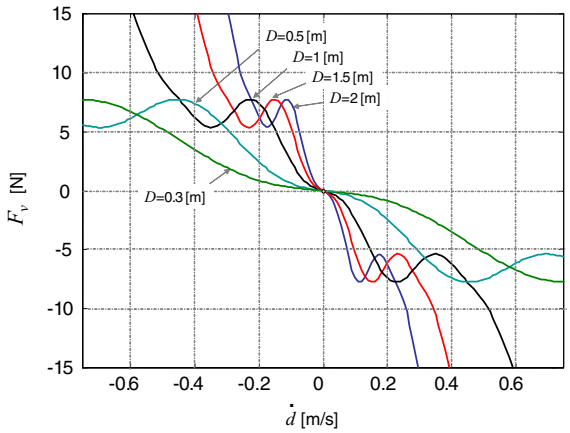

Fig. 5 Drag force characteristic for different diameters

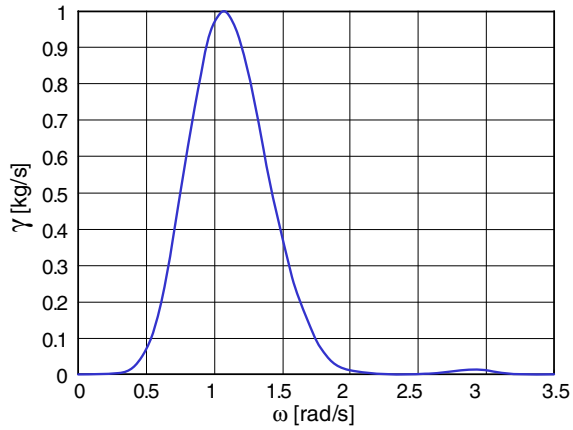

Fig. 6 Potential damping of a submersed spherical body with $D = 2$ and $d = 15$ m

Figure 5 describes the drag force characteristic based on the relation $F_v = -[(\pi\rho D^2)/(8)]C_D(\dot{d})\,\dot{d}|\dot{d}|$ is described for different volumes.

2.3 Equations of motion: Model 3

A better characterization of the cable-ROV dynamics will include the radiation capability of the submersed body in motion. The radiation is significant mainly at lesser immersion depths. It declines exponentially with increasing d.

In this situation, the dynamics are affected by a new force, namely the so-called induced-radiation force given by

$$F_r(t) = -m_\infty \ddot{d}(t) - \int_{-\infty}^{t} \kappa(\tau; D, d)\, \dot{d}(t-\tau)\, d\tau, \tag{11}$$

where $\kappa(\tau; D, d)$ is an impulse-response function accounting for the memory of the fluid response to a sudden body displacement. It depends on the geometry of the wet part of the submersed body as well as on the immersion depth. For a sphere, the geometry is parametrized by D.

A straightforward method to calculate κ is the so-called damping function

$$\kappa(\tau; D, d) = \frac{2}{\pi}\int_0^\infty \gamma(\omega; D, d)\, \cos(\omega t) d\omega, \tag{12}$$

where $\gamma(\omega; D, d)$ is the potential-damping function parametrized in D and d. It can be calculated numerically using Strip Theory and Flow Potential Theory (cf. [14]). For instance, Fig. 6 shows the potential-damping function of a spherical body for particular values of $D = 2$ and $d = 15$ m. This was obtained with the tool AQWA® for hydrodynamics computation [1].

The dependency of γ on D and d for $d > D/2$ can be approximated by

$$\gamma(\omega; D, d) = f(D, d) \quad \gamma(g(d)\omega; 2, 15), \tag{13}$$

with attenuation and contraction functions

$$f(D, d) = 4.8 \times 10^6 \frac{D^{4.58}}{(d + 7.05)^6} \tag{14}$$

$$g(d) = \frac{8.28}{(d + 2.51)^{0.73}}, \tag{15}$$

respectively. Relations (14) and (15) were obtained by interpolating various curves $\gamma(\omega; D, d)$ for a set of values of D and d and normalizing with respect to $\gamma(\omega; 2, 15)$.

Using Fig. 6 and putting Equation (13) into Equation (12), the impulse-response function is numerically found. Figure 7 shows different impulse-response functions for a set of values of D and d. One concludes the importance of the response for low depths and relatively large diameters. Other feature of the model is the oscillating evolution of the response with a resonance frequency that decreases with the depth.

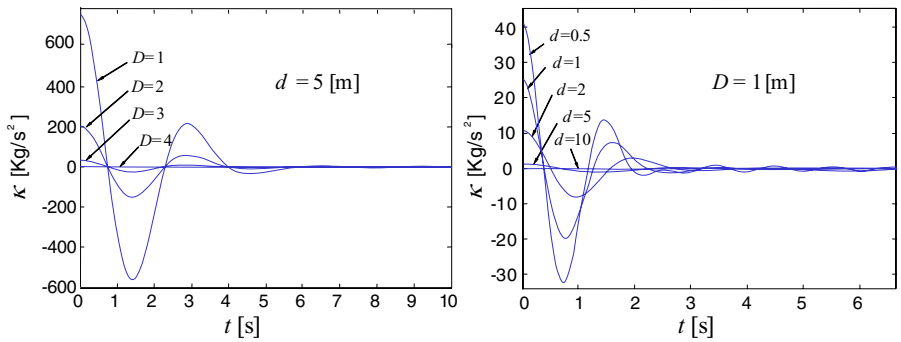

Fig. 7 Impulse responses for different diameters D and depths d

After calculating $\kappa(\tau; D, d)$ for the body diameter and depth, (11) can be applied so as to evaluate the induced-radiation force F_r for the sinking/lifting process.

As d is a system state, the impulse response becomes time dependent

$$\kappa(\tau, t) = \kappa(\tau, d(t)) \tag{16}$$

Thus, the equations of motion in vertical z-axis become first for the taut condition

$$[m + m_\infty]\,\ddot{d} + \frac{\pi\rho D^2}{8} C_D(\dot{d})\,\dot{d}|\dot{d}| + \frac{EA_0}{L}(d - L + b) + \frac{\pi\rho D^3}{6} g + F_t = mg + \frac{EA_0 a}{L}\sin(\omega t) - \int_{-\infty}^{t} \kappa(\tau, t)\,\dot{d}(t-\tau)\,d\tau, \tag{17}$$

and for the slack condition

$$[m + m_\infty]\,\ddot{d} + \frac{\pi\rho D^2}{8} C_D(\dot{d})\,\dot{d}|\dot{d}| + \frac{\pi\rho D^3}{6} g + F_t = mg - \int_{-\infty}^{t} \kappa(\tau, t)\,\dot{d}(t-\tau)\,d\tau. \tag{18}$$

Notice that

$$f_0 = -\int_{-\infty}^{0} \kappa(\tau, 0)\,\dot{d}(t-\tau)\,d\tau, \tag{19}$$

describes the effect of the past evolution of the hydrodynamics at $t = 0$, i.e., the initial condition for the differential Equations (17) and (18). Fortunately, the evanescence of $\kappa(\tau)$ for $\tau \to \infty$ and the passivity of system (17) and (18) indicate that the fact of supposing $f_0 = 0$ has no effect on the accuracy of the solution $d(t)$ at steady state (see [12]). So, for the following studies in steady state, it is assumed null.

3 Stability analysis

An attempt to obtain an analytical solution for the different nonlinear Equations (4), (5), (9), (10), (17), and (18) generally fails. The motion equations can be put generically as

$$\ddot{d} + f(\dot{d}, d, \mu_i) = h(u, \mu_j), \tag{20}$$

where $u = a\sin(\omega t)$ is the input, f is a function containing the nonlinear stiffness and damping, and h is a nonlinear input function. The coefficients represented by μ_i and μ_j are free parameters that influence the features of the behavior and are transcendent for accounting for physical changes in the cable properties like premature fatigue strength or fracture. For instance, the existence of conditions for period-1 solutions and approximated methods of solution are discussed in Rossenwasser [20] and Guckenheimer and Holmes [5].

Huang [9] established an analytical procedure for detecting the stability of forced period-1 stable orbits based on the observation of eigenvalues of a discrete system that relates cross points through zero of periodic orbits. The method is complemented with an iterative algorithm for enhancing the information given by the eigenvalues about stability. The domain of attraction is extremely sensitive to bad initial conditions, so that the result is not always reliable to be extended here.

In this paper, we develop numerical procedures in order to establish stability. These are based on Poincaré maps, time averaging, and asymptotic measures [5].

3.1 Periodic solutions

Let us assume that the behavior of the umbilical–ROV system starts from an initial condition $(d(0), \dot{d}(0))$ and its state trajectory sampled at a rate $T = (2\pi/\omega)$. The resulting time-discrete dynamics is described by

$$\begin{bmatrix} d(k+1) \\ \dot{d}(k+1) \end{bmatrix} = \mathbf{F}\left(\begin{bmatrix} d(k) \\ \dot{d}(k) \end{bmatrix}, \mu \right). \tag{21}$$

where k is a positive integer, $\mathbf{F}$ a nonlinear vector-valued function that is smooth in both regions delimited by $d - L + b - a\sin(\omega t) > 0$ and $d - L + b - a\sin(\omega t) \leq 0$, and μ a vector that describes the control parameters for bifurcation analysis. These parameters conform a complete space for searching stability regions, i.e., regions that are free of taut–slack motions for given initial conditions in an attraction domain.

The exact determination of $\mathbf{F}$ rests on the analytical availability of solutions of (4) and (5) (or (9), (10) or (17), and (18)), which is only possible in the slack motion in (5) by analytically solving Bernoulli-type differential equations. For this reason, we attempt to follow a numerical way instead.

3.2 Identification of periodic solutions

Periodic orbits of the continuous systems (4), (5), (9), (10), (17), and (18) correspond to a fixed point of the discrete system (21) described in the Poincaré map.

So, for a particular valued μ, there exists a solution $d(t)$ and a state trajectory that starts from an arbitrary initial condition $\zeta(0)$ in an attraction domain and is asymptotically periodic with period $nT = (n2\pi/\omega)$.

Considering the sampled trajectory conformed as

$$\zeta(k) = \begin{bmatrix} \zeta_1(k) \\ \zeta_2(k) \end{bmatrix} = \begin{bmatrix} d(t_0 + kT) \\ \dot{d}(t_0 + kT) \end{bmatrix},$$

we say the system is asymptotically stable and has a fixed point when the series $\{\zeta(k)\}_{k=0}^{\infty}$ converges to a periodic series. Moreover, there exists a sufficiently large delay q such that $\{\zeta(k) - \zeta(k-q)\}_{k=0}^{\infty}$ is a Cauchy series.

In order to detect the periodicity nT of $\zeta(k)$ during the transient state, one takes two positive test integers q and n, with $q/n \gg 1$ and some small real-valued ε. Thus, if $\zeta(k)$ is nT periodic, then there exists a sample time k_0 from which onward, i.e., up to $k \geq k_0$, following relations are fulfilled

$$\begin{cases} \|\zeta(k) - \zeta(k-1)\| > \varepsilon \\ \vdots \\ \|\zeta(k) - \zeta(k-n+1)\| > \varepsilon \\ \|\zeta(k) - \zeta(k-n)\| < \varepsilon \\ \|\zeta(k) - \zeta(k-n-1)\| > \varepsilon \\ \vdots \\ \|\zeta(k) - \zeta(k-2n+1)\| > \varepsilon \\ \|\zeta(k) - \zeta(k-2n)\| < \varepsilon \\ \|\zeta(k) - \zeta(k-2n-1)\| > \varepsilon \\ \vdots \\ \|\zeta(k) - \zeta(k-q)\| > \varepsilon. \end{cases} \tag{22}$$

and the series of the previous system within the band ε will also accomplish

$$\lim_{k\to\infty} \|\zeta(k) - \zeta(k - v\,n)\| = 0, \tag{23}$$

for $v = 0, \pm 1, \pm 2, \ldots$. Moreover, (22) and (23) are independent of t_0, except for a set with measure zero of series that are identically zero or constant.

Equation system (22) is equivalent to the autocorrelation function $\vartheta(\tau) = \sum_{k=0}^{\infty} \zeta(k)\zeta^T(k+\tau)$ for $\tau = 0, 1, \ldots$. The cadency of peaks of $\vartheta(\tau)$ for large τ will reveal the periodicity of ζ.

The detection method developed above can also be used to identify a chaotic state. In this case, there does not exist any finite integer q that satisfies (22). Assuming the system is in stationary state, the chaos condition means

$$\lim_{q\to\infty} \|\zeta(k) - \zeta(k-j)\| > 0, \quad \text{with } j = 0, \ldots, q, \tag{24}$$

i.e., no series $\{\zeta(k) - \zeta(k-j)\}_{k=0}^{\infty}$ is a Cauchy series. Moreover, in this case, $\vartheta(\tau) \neq 0$ for all τ except, perhaps, for a countable set of measure zero.

It is observed that the detection method proposed above performs well in the transition from the transitory to the steady state. The application of the identification method is illustrated in Fig. 9 for a period-4 behavior of the cable–ROV system with free

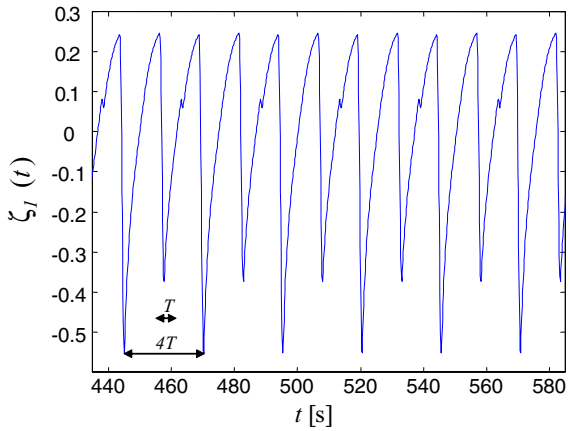

Fig. 8 Period-4 behavior of the ROV dynamics

parameter: $D = 0.85\,\text{m}$, $EA_0 = 5 \times 10^6\,\text{N}$, and $C_\text{D} = 0.2$, time evolution for which is depicted in Fig. 8.

The detection of this period is performed on the sampled series on $\zeta_1(t)$ of Fig. 8 at a rate equal to the wave period $T = 6.5\,\text{s}$.

According to the restrictions (22) and for a tolerance selected as

$$\varepsilon = 10^{-6} \max_{t\in[0,\infty],\tau\in(0,\infty]} |\zeta(t) - \zeta(t-\tau)|$$
$$= 10^{-6}\left(\max_{t\in[0,\infty]} \zeta(t) - \min_{t\in[0,\infty]} \zeta(t)\right), \tag{25}$$

four series are analyzed, namely the ones for $n = 1$ up to $n = 4$, where period 4 is established through the convergence testing, see Fig. 9. Also, the series for $n = 8$ produced a Cauchy series during the stability analysis, but the first series detected by the method was for $n = 4$. This concludes the fixed point period 4 for the set of free parameters.

4 Stability regions

In this paper, a stability region is defined as a zone in the free-parameter space, in which the behavior of the umbilical–ROV system is characterized by a bounded oscillation in steady state subject to the taut condition $F_\text{c} > 0$. From a practical point of view, such regions characterize predictable and safe ROV operations.

The boundary of a stability region depends on the initial vector $(d(0), \dot{d}(0))^T$, which is assumed to be equal to $(L(0) - b, 0)^T$ in the set of experiments. For specific values of free parameters, the dynamics can also bifurcate, showing high period oscillations or even chaos. To find stability regions, the three models stated earlier will be employed.

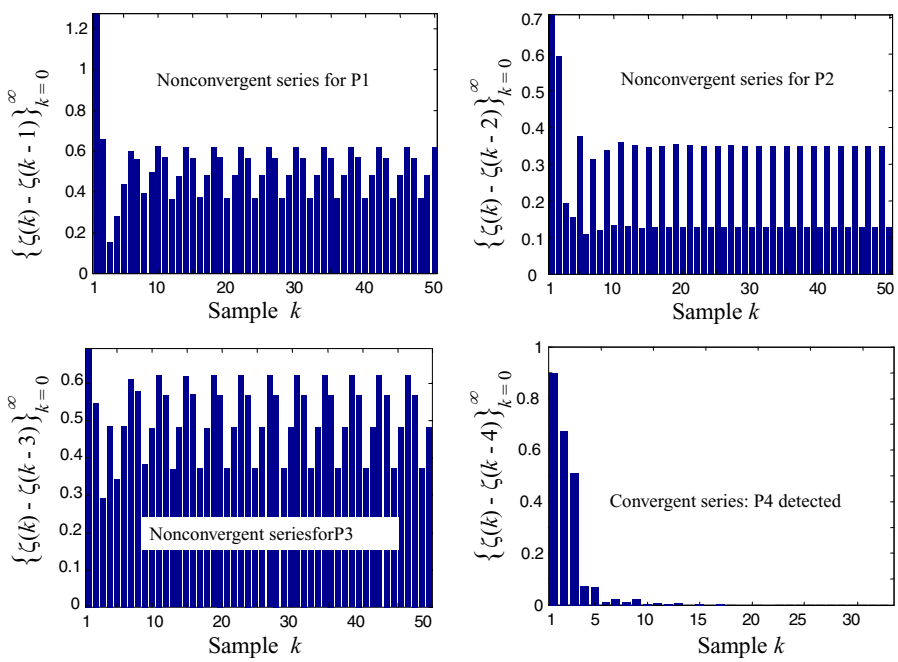

Fig. 9 Detection of bifurcations for a period-4 case upon Cauchy series

Table 1 Design and operation parameters

Design	Operation
D: ROV diameter	L: cable length
A_0: cable cross section	ω: wave frequency
m: ROV mass	a: wave amplitude
C_{D}(shape): drag coefficient	$C_{\mathrm{D}}(Re)$: drag coefficient
m_∞: added mass	F_{t}: vertical thruster force
E: Young's modulus	b: crane jib elevation

4.1 Free parameters

First, let us distinguish between design and operation parameters, i.e., those that are fixed in the ROV design and those that may vary during the operation. These are listed in Table 1.

Most of them are suitable for the study of nonlinear oscillations, i.e., the system behavior changes significantly with respect to those parameters. So, we define the parametric space for stability regions with a set of them conforming the vector

$$\mu = [D, EA_0, C_{\mathrm{D}}(\text{shape}), C_{\mathrm{D}}(Re), L, F_{\mathrm{t}}, a, \omega]^T. \tag{26}$$

The ROV mass m and added mass m_∞ are not directly employed in (26) but through the relations $[(m)/(\rho\{\pi D^3/6\})] = c_1 > 1$ and $[(m_\infty)/(\rho\{\pi D^3/6\})] = c_2 = 0.5$, respectively, with c_1 and c_2 being specified constants.

In order to perform simulations for several kinds of operations and for a wide class of umbilical–ROVs with spherical shell, the basic settings are prescribed mostly in intervals (see Table 2).

Due to the large dimension of the free-parameter space, stability regions are constructed in subspaces conformed by pairs of components of μ, while each of their complement is maintained constant. In order to identify the kind of oscillation, particular stability regions are shaded so as to indicate orbits with the same periodicity. Also, each orbit is depicted with a symbol that identifies its periodicity. The detection of periodicity is performed according to the identification method developed previously on the basis of Cauchy series for a tolerance given by (25).

4.2 Stability according to model 1

To study the taut–slack phenomenon and its stability properties, simulations are carried out on the basis of the models (4) and (5).

Figures 10–16 illustrate the stability region in different subspaces corresponding to an experiment series for a constant drag coefficient, which is the main particularity of model 1. Generally speaking, it is seen that the stability region is composed by definition of behaviors of periodicity 1, termed P1, with a taut condition fulfilled. Outside the stability region, the diversity of behavior is wide, ranging from P1 up to chaos. The presence of period doubling is not a characteristic of the stability regions, as, for instance, this occurs in related ODEs like the Mathieu and Duffing quadratic nonlinear differential equations. The reason for this is the presence of two actuating nonlinearities, i.e., the bilinear and the quadratic characteristics for the cable force and the drag, respectively. Moreover, the behavior diversity in the subspace is characterized with both odd- and even-high-period oscillations. This suggests different scenarios of the routes to chaos.

Figure 10 shows the role of the monochromatic wave excitation through its parameters a and ω on the system stability. It is seen that large wave steepness, i.e., $(a\omega)$ leads to the phenomenon taut–slack with chaos as one of the most common behavior in this subspace. The band between the stability region and chaos is thin and composed mostly of oscillations P1 and P2.

Figure 11 demonstrates the balance between the ROV mass through D and cable stiffness for a middle cable length. Accordingly, one sees that the

Table 2 Basic simulation parameters

Design parameters	Span	Operation parameters	Span
$D = 1\,\mathrm{m}$	[0.5:2]	$L = 50\,\mathrm{m}$	$[1{:}10^2]$
$EA_0 = 10^6\,\mathrm{N}$	$[10^5 : 10^7]$	$\omega = 1\,\mathrm{rad/s}$	$[10^{-1} : 5]$
$\frac{m}{\rho\frac{\pi D^3}{6}} = 1.1$	–	$a = 1\,\mathrm{m}$	[0:3]
C_{D} (shape) $= 0.2$	–	$C_{\mathrm{D}}(Re)$	See Fig. 3
$b = 3\,\mathrm{m}$	–	$F_{\mathrm{t}} = 0\,\mathrm{N}$	[−600:600]

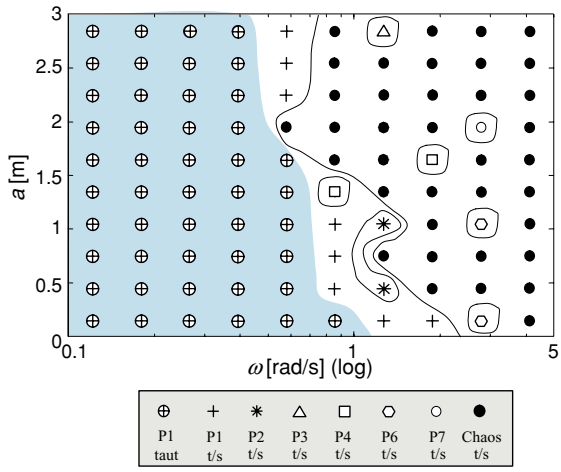

Fig. 10 Stability region: wave amplitude vs. frequency for $C_D = 0.2$, $EA_0 = 10^6$ N, and $L = 50$ m

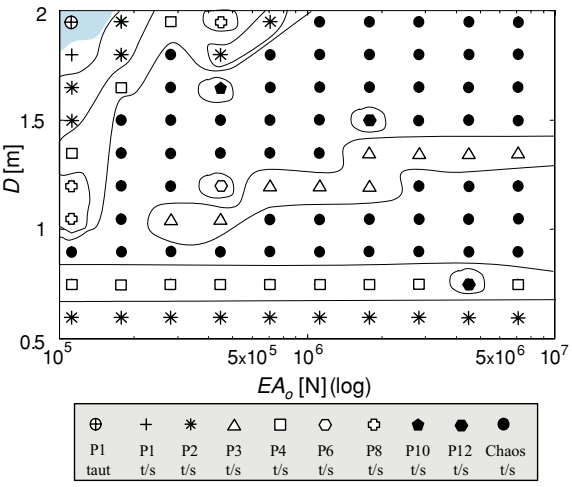

Fig. 11 Stability region: ROV diameter vs. cable stiffness constant for $C_D = 0.2$, $a = 1$ m, $\omega = 1$ rad/s, and $L = 50$ m

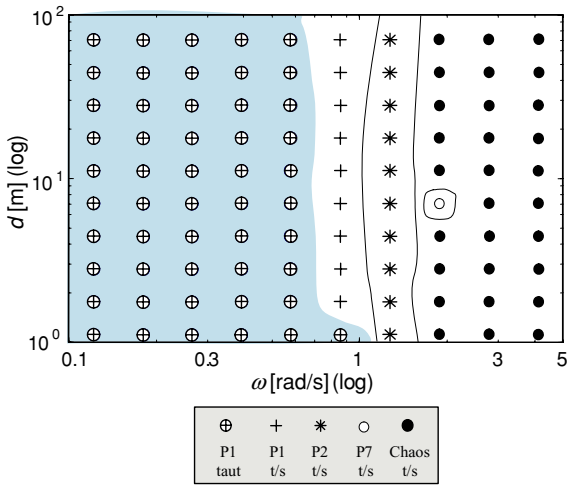

Fig. 12 Stability region: ROV depth vs. frequency for $C_D = 0.2$, $a = 1$ m, and $EA_0 = 10^6$ N

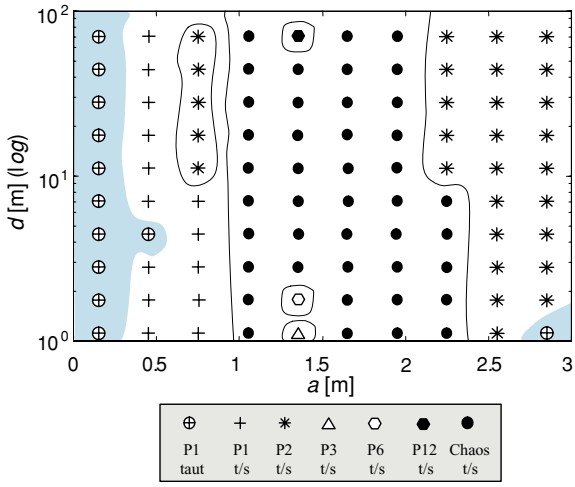

Fig. 13 Stability regions: ROV depth vs. wave amplitude for $C_D = 0.2$, $\omega = 1$ rad/s, and $EA_0 = 10^6$ N

larger the diameter of the ROV, the more elastic the cable has to be in order to avoid the taut–slack condition.

Figure 12 shows a marked insensitivity of the oscillation with depth. This occurs inside and outside the stability region, except for superficial depths, for which the stiffness is high, i.e., where L is small. Generally, if L is smaller and the stiffness larger, it is more feasible that the ROV can follow the harmonic motion of the jib. Conversely, the behavior shows a great sensibility to wave frequency.

A similar insensitivity, yet not so pronounced as in the case before, is encountered in the relation of the depth with the wave amplitude, see Fig. 13. It is noticed that a second portion of the stability region emerges at the right side of the picture for large a and small L. This suggests a disconnection of both stable portions in the subspace considered.

Figure 14 shows the effect of the ROV thrust and the wave excitation on the system behavior about a fixed depth. Clearly, when $F_t > 0$ (i.e., the ROV is pulled down), it is valid that the larger the thruster power, the larger would be the stability region, even for increasing wave amplitudes. Conversely, for the thrusters actuating in the other direction (see at $F_t < 0$), the ROV is pulled to the surface and the slack condition arises for

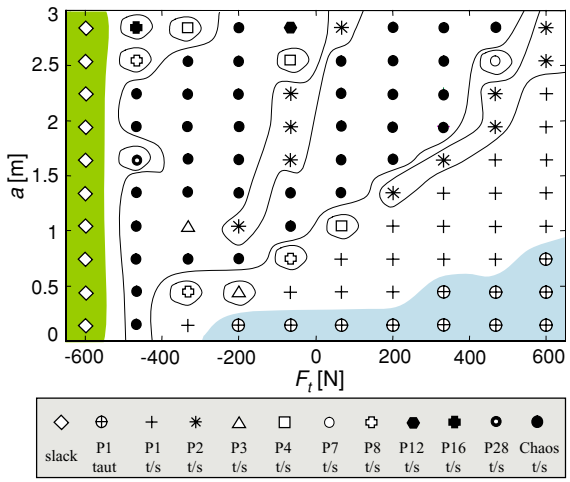

Fig. 14 Stability region: wave amplitude vs. thruster force for $C_D = 0.2$, $\omega = 1$ rad/s, $EA_0 = 10^6$ N, and $L = 50$ m

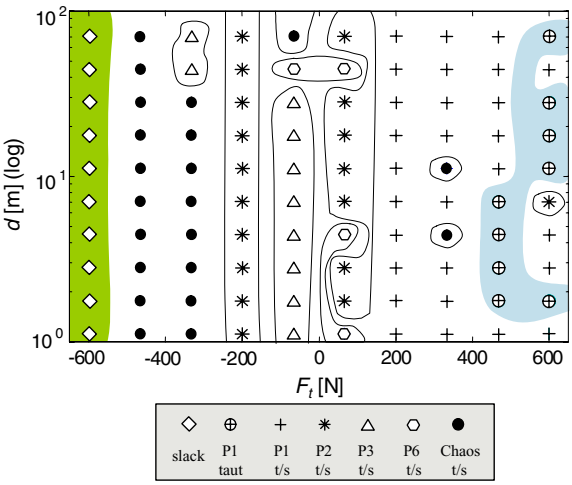

Fig. 15 Stability region: ROV depth vs. thruster force for $C_D = 0.2$, $a = 1$ m, $\omega = 1$ rad/s, and $EA_0 = 10^6$ N

large F_t. This indicates unstable orbit but unbounded behavior.

Figure 15 illustrates the effect of the thruster force on the stability at different depths. It is seen that stable oscillations occur when the actuators can maintain sufficiently large cable tension. The same as before is said for the portion shaded as slack.

The last figure, Fig. 16, depicts similar results as Fig. 14, i.e., the stability region enlarges for increasing ω and F_t. In general, both figures indicate the fact that with increasing wave energy in the system (e.g., increasing wave steepness) the only way to circumvent the taut–slack phenomenon is to strengthen the cable

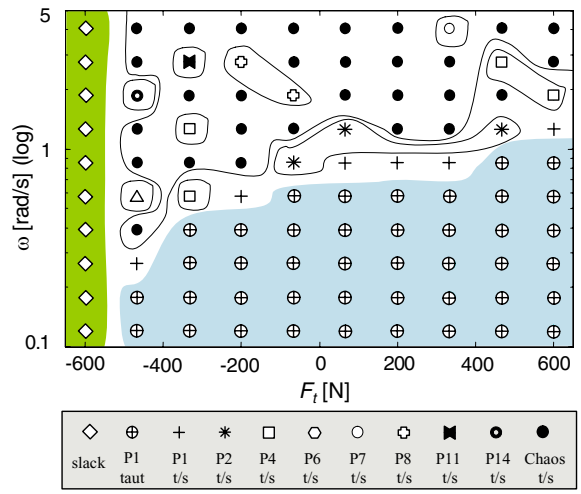

Fig. 16 Stability region: wave frequency vs. thruster force for $C_D = 0.2$, $a = 1$ m, $EA_0 = 10^6$ N, and $L = 50$ m

by investing more power in the actuators. Later, we will illustrate an application of a control system that can accomplish this goal in which thruster and hoisting crane will play an important role as actuators to ensure stability.

4.3 Stability according to model 2

In this section, model (9) and (10) are considered with the same setup for simulations as in model 1. The main improvement of model 2 in comparison to model 1 is the incorporation of a variable drag coefficient with motion dependence. The experiments are illustrated in Figs. 17–23.

In general, it is noticed, that the diversity of orbits is qualitatively broader than in the cases handled before. This feature was expected due to the complexity of the nonlinear drag characteristic. Additionally, it is worth noticing that the limits of the stability regions remain almost the same as in the earlier case. Particular differences will be exalted comparatively with respect to homologous pictures of model 1.

Figure 17 shows similitudes in the behavior diversity with respect to the homologous case in Fig. 10, above all, in the zone of small steepness ($a\omega$), just where the motion is not too significant, and accordingly the drag coefficient does not vary too much. This coincidence is also observed outside the stability region at many points in which ($a\omega$) is considered relatively small.

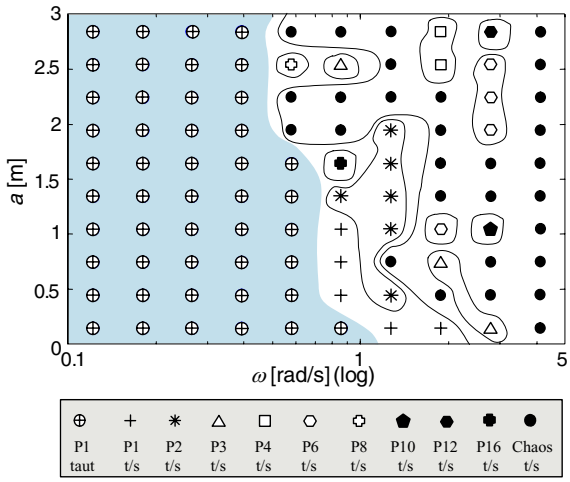

Fig. 17 Stability region: wave amplitude vs. frequency for C_D variable, $EA_0 = 10^6$ N, and $L = 50$ m

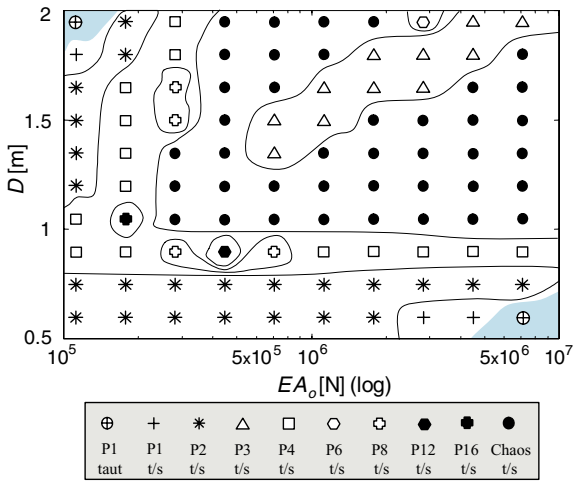

Fig. 18 Stability region: ROV diameter vs. cable stiffness constant for C_D variable, $a = 1$ m, $\omega = 1$ rad/s, and $L = 50$ m

Similar conclusions are worked out from Fig. 18 with respect to Fig. 11. An obvious difference is the enlargement of the stability region for small D and large stiffness.

Figure 19 illustrates a marked insensitivity of the oscillation with respect to the length. The difference here with respect to the homologous case in Fig. 12 is that the diversity in the frequency is higher.

Similar conclusions are deduced from Fig. 20 with respect to Fig. 13. The variant here is that the chaotic zone is broader, and periodic solutions of odd periodicity are more common, whereas in the previous homologous case, the solutions were mostly of even period.

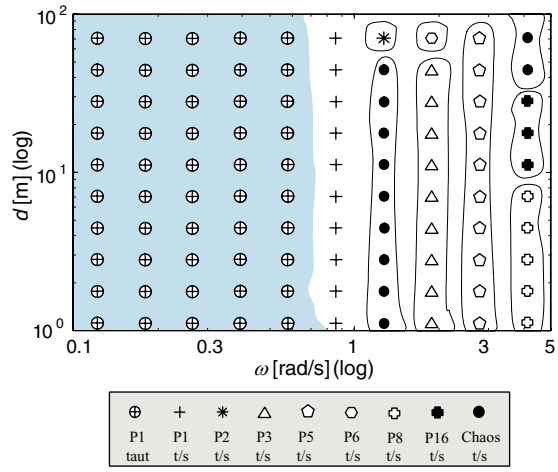

Fig. 19 Stability region: ROV depth vs. frequency for C_D variable, $a = 1$ m, $\omega = 1$ rad/s, and $EA_0 = 10^6$ N

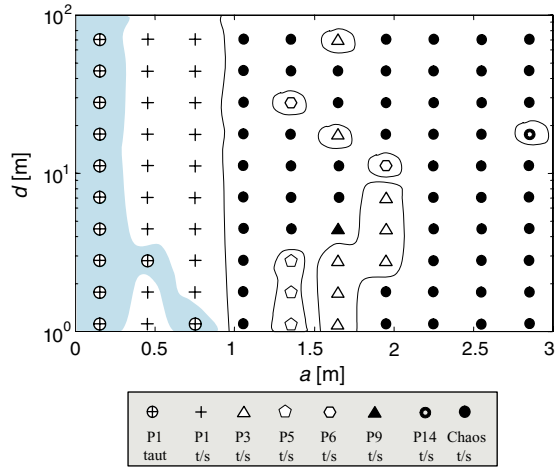

Fig. 20 Stability regions: ROV depth vs. wave amplitude for C_D variable, $\omega = 1$ rad/s, and $EA_0 = 10^6$ N

Figure 21 and the related homologous Fig. 14 are similar. In addition to a qualitatively more varied scene, it worth mentioning that the stability region and its adjacent band of P1 solutions are wider than in the homologous case mentioned earlier.

The two next figures, Figs. 22 and 23, illustrate the influence of the thruster force on the stability in relation to L and a, respectively. The stability regions are slightly different in comparison to those of their homologous cases in Figs. 15 and 16. However, the differences are significant outside the regions. Nevertheless, the order of the diversity in homologous cases is not too different.

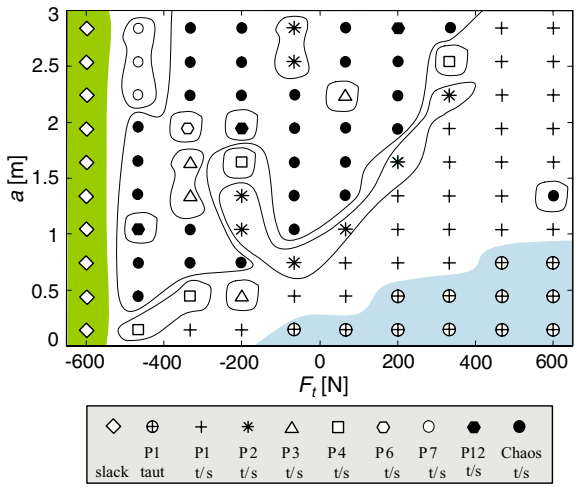

Fig. 21 Stability region: wave amplitude vs. thruster force for C_D variable, $\omega = 1$ rad/s, $EA_0 = 10^6$ N, and $L = 50$ m

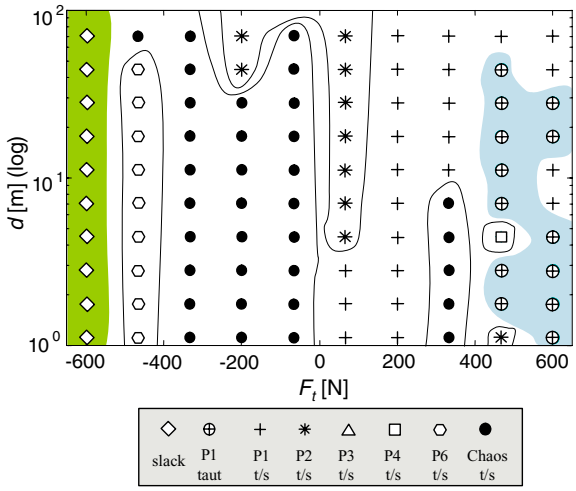

Fig. 22 Stability region: ROV depth vs. thruster force for C_D variable, $a = 1$ m, $\omega = 1$ rad/s, and $EA_0 = 10^6$ N

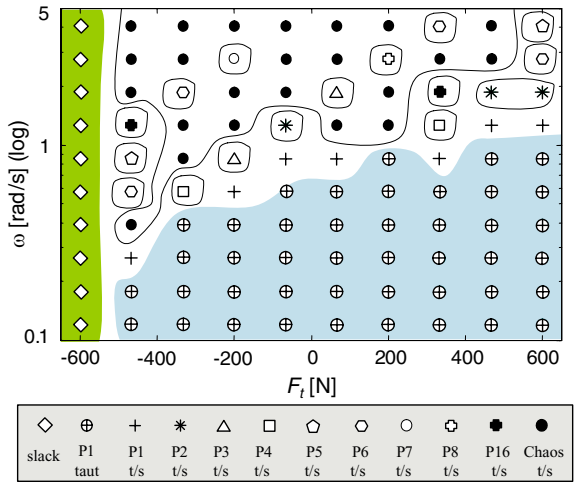

Fig. 23 Stability region: wave frequency vs. thruster force for C_D variable, $a = 1$ m, $EA_0 = 10^6$ N, and $L = 50$ m

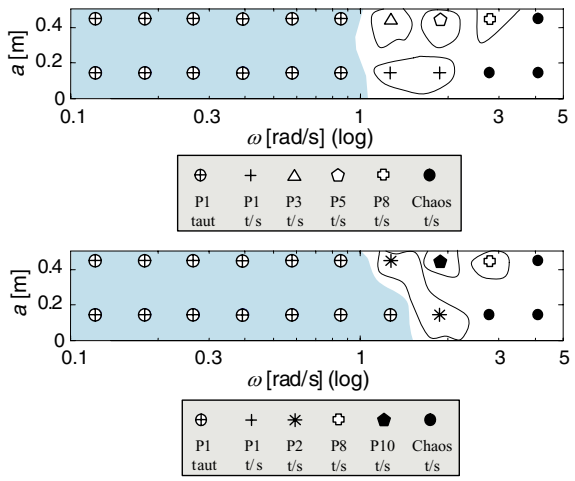

Fig. 24 Stability regions: wave amplitude vs. wave frequency for C_D variable, $EA_0 = 10^6$ N, and $L = 4$ m. (*Top*) Simulation without radiation force. (*Bottom*) Simulation with radiation force

4.4 Stability according to model 3

Finally, model (17) and (18) is simulated under the same scheduling as the former models. Apart from having a motion-dependent drag coefficient like model 2, the improvement provided by this model is the consideration of the potential radiation force F_r. As this force is significant mainly for shallow waters, the experiments are focused on lesser depths varied stepwise from 1 up to 5 m. The stability region is investigated in the subspace a versus ω only. The pictures of model 3 and its homologous from model 2, both are put in the same frame for direct comparison.

Figure 24 considers the oscillatory behaviors at a depth of 1 m. The stability region enlarges comparatively slightly with consideration of F_r, but the diversity outside this region is different in the periodicity. However, the chaotic behaviors remain in the same positions in the space.

Figure 25 depicts a scenario at a depth $d = 2$ m. This is characterized by equal stability regions with and without F_r and almost identical variations in the periodicity in both the cases. The chaotic region is comparatively slightly different.

Figure 26 illustrates the periodicity at a depth $d =$ 5 m comparatively. The stability regions are slightly

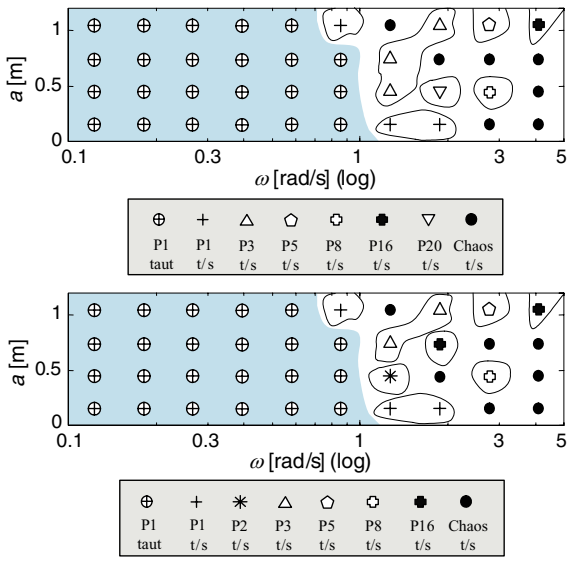

Fig. 25 Stability regions: wave amplitude vs. wave frequency for C_D variable, $EA_0 = 10^6$ N, and $L = 5$ m. (*Top*) Simulation without radiation force. (*Bottom*) Simulation with radiation force

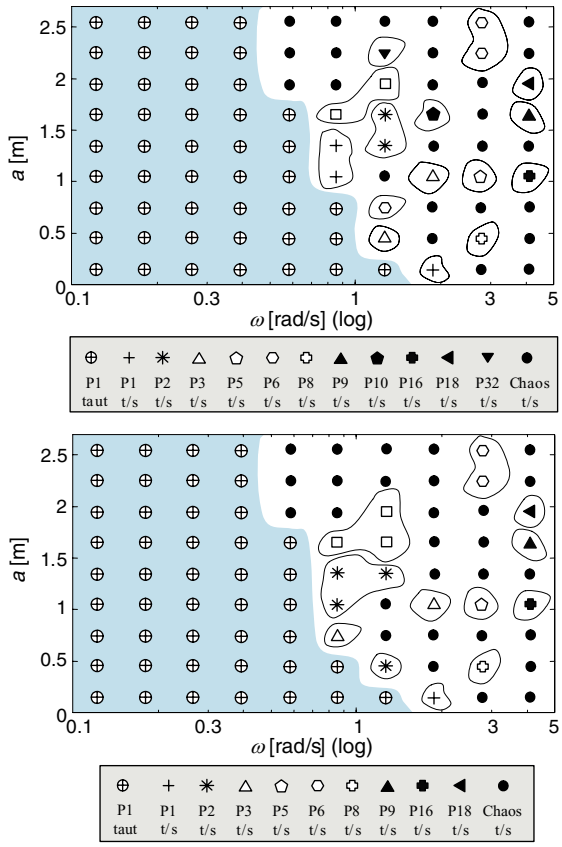

Fig. 26 Stability regions: wave amplitude vs. wave frequency for C_D variable, $EA_0 = 10^6$ N, and $L = 8$ m. (*Top*) Simulation without radiation force. (*Bottom*) Simulation with radiation force

different. Also, the regions with presence of chaos are very similar. The periodicity changes at some specific points only; however, it is not so abrupt when considering F_r.

We can conclude that radiation forces have an insignificant influence in the system dynamics for depths $d \geq 5$ m. As the usual depths of the ROV in the operation are much larger than this limit, it is inferred that model 2 is sufficiently accurate for the analysis intended in this paper.

5 Taut/slack control

In the sinking/lifting operation, the taut state of the cable describes actually the less stressed condition from the viewpoint of magnitude of strength and fatigue. This can be inferred from a case study in Fig. 27, where the evolution of the cable force is shown to travel from the taut through the taut–slack state. This qualitative change occurs during the transient behavior and is typically characterized by abrupt and hefty increments of the force magnitude due to accelerations of the upper extreme of the cable during the slack condition followed by violent yanks when the cable tows the ROV again. This scenario takes place at higher frequencies, depending of the natural frequency of the mass–spring system constituted by ROV and cable. The shorter the cable length, the larger will be the frequency of the taut–slack state evolution. Also, the maximal magnitude of the force in the taut–slack condition depends directly on the magnitude of the wave steepness ($a\omega$).

Another advantage of preserving the taut state in the operation is the more predictable evolution of the ROV trajectory than under the taut–slack state. From Figs. 10–23, it is clearly seen that the system behavior is always periodic P1 in the taut condition and that generally this periodic evolution turns unstable with high periods inclusive of chaos under the presence of the taut–slack phenomenon.

Bearing in mind the mentioned advantages, an appropriate control law for the sinking/lifting process is consequently given to care for the limit cable stress and simultaneously to maintain the taut condition. Additionally, a practical requirement by the descent or ascent of the unit is to minimize the times required for these operations.

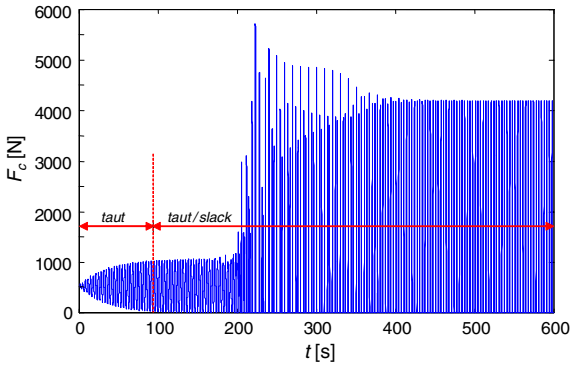

Fig. 27 Evolution of the cable force for a wave amplitude $a = 0.1$ m, frequency $\omega = 1.87$ rad/s, stiffness constant $EA_0 = 10^6$ N, and cable length $L = 50$ m

To achieve these control objectives, the hoisting crane system and the ROV thrusters are involved in a controller design. They must properly be synchronized in a simultaneous, optimal, and secure form for reaching the desired depth in short times. In return, it would be expected that the benefit of any controlled operation be a significant extension of the stability regions with respect to the uncontrolled system.

To this end, the control system can be conceived as a dynamic system with two inputs, namely the set points d_{ref} and $F_{c_{\text{ref}}}$ for depth and a suitable cable strength, respectively, and an unavoidable wave perturbation $a\sin(\omega t)$. However, it would have three measurable outputs, namely the ROV velocity $\dot{d}$, the cable length L, and the cable tension F_c (see Fig. 28).

So, the control strategy can be achieved with the help of two mechanisms. First, the cable tension is regulated from both extremes using controllers on the crane motor and the ROV thrusters, respectively. Second, in order to track the desired trajectories for ascent/descent fast and accurately, the ROV velocity is controlled separately. All controllers are nonlinearly coupled through multiple feedbacks, as seen from the proposed structure in Fig. 28.

Notice that the main cause of the taut–slack phenomenon is the wave perturbation. Higher the energy of the wave, the more accentuated is the phenomenon. For monochromatic waves, the mean energy is proportional to $(\omega a)^2$. Since the actuators can produced a limited energy for reaching levels of thrust and velocity, the effectiveness of any control system will be obviously restrained by a specified maximal wave steepness (ωa).

5.1 Nonlinear control law

To achieve the control goal, a 2-degree-of-freedom control law is proposed with a control action vector

$$\mathbf{u}(t) = [u_t(t), u_{cr}(t)]^T, \tag{27}$$

where u_t is the thruster voltage and u_{cr} the crane motor voltage (see Fig. 28).

The set point for cable stress $F_{c_{\text{ref}}}$ is defined as a fraction of the fracture tension. The cable force has to be dynamically regulated around this set point, avoiding the slack of the cable.

Considering model 2, the nonlinearities of the dynamics in the terms of Equations (9) and (10) are included in the forces and moments, namely

$$F_v = -\frac{\pi\rho D^2}{8} C_D(\dot{d})\,\dot{d}|\dot{d}| \tag{28}$$

$$F_c = \begin{cases} -\dfrac{EA_0}{L} z, & \text{for } z \geq 0 \\ 0, & \text{otherwise} \end{cases}, \quad \text{with}$$

$$z = d - L + b - a\sin(\omega t) \tag{29}$$

$$F_t = \begin{cases} \dfrac{K_t}{s^2+\gamma_1 s+\gamma_0} u_t|u_t|, & \text{for } u_t \in [u_{t\,\min}, u_{t\,\max}] \\ F_{t\,\min}, & \text{for } u_t \leq u_{t\,\min} \\ F_{t\,\max}, & \text{for } u_t \geq u_{t\,\max} \end{cases} \tag{30}$$

$$M_{cr} = \begin{cases} \dfrac{k_1 s}{\frac{L_a J}{k_1 k_2} s^2 + \frac{R_a J}{k_1 k_2} s + 1} u_{cr}, & \text{for } u_{cr} \in [u_{cr\,\min}, \\ & \quad u_{cr\,\max}] \\ M_{cr\,\min}, & \text{for } u_{cr} \leq u_{cr\,\min} \\ M_{cr\,\max}, & \text{for } u_{cr} \geq u_{cr\,\max} \end{cases}, \tag{31}$$

where γ_0 and γ_1 are coefficients of the thruster motor dynamics, K_t is its gain, M_{cr} the moment of the crane drum, L_a and R_a the armature inductance and resistance of the crane motor, respectively, J the moment of inertia, r the radius of the wrapping drum, k_1 the transfer gain between the armature current and the drum angular acceleration, and k_2 the transfer gain between the drum angular speed and the back emf. The coefficients, $u_{t\,\min}$, $u_{t\,\max}$, $u_{cr\,\min}$, and $u_{cr\,\max}$ are the limiting saturation values of the thrusters and crane motor, respectively.

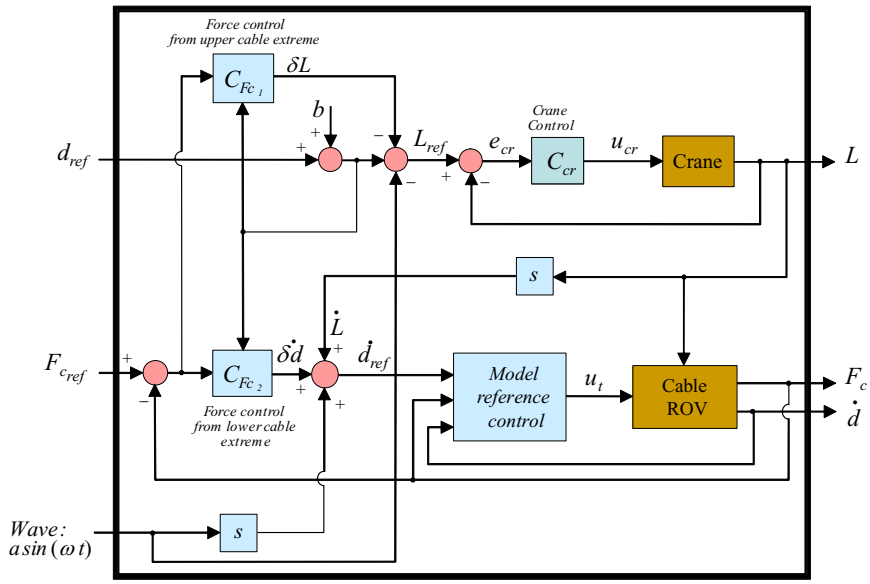

Fig. 28 Control of depth and cable tension in lowering/lifting operation of a ROV

The nonlinearity (28) is nonconvex over an interval that depends on the ROV diameter (see Fig. 5). Additionally, it is only two times derivable with respect to $\dot{d}$ because of the singularity at $\dot{d} = 0$. Similarly, it occurs with the nonlinearities (29) and (30), whose high derivatives do not exist at $z = u_t = 0$ with respect to z and u_t, respectively. Because of the lack of smoothness, nonlinear controls based on differential geometry cannot be applied to achieve the control objectives. However, a great part of such nonlinear dynamics can be cancelled using nonlinear feedback, as shown next.

To regulate the cable tension, two controllers are employed, one for each extreme (see Fig. 28). The cable force controllers are driven by the force error $e_f = F_{c_{ref}} - F_c$ and generate corrections termed as $\delta\dot{L}$ and $\delta\dot{d}$ for the crane system and the ROV thrusters, respectively.

For these specific tasks, the equilibrium stress point of the cable given by the restriction

$$\dot{d} - \dot{L} - a\omega\cos(\omega t) = 0, \tag{32}$$

is modified to

$$\dot{d} - \dot{L} - a\omega\cos(\omega t) = \delta\dot{d}, \tag{33}$$

with the property

$$\int_0^\infty |\delta\dot{d}|dt = c_1 \tag{34}$$

and $c_1 > 0$ being a constant for a bounded response. In this way, the lower point of the cable is then tensed conveniently by selecting the function $\delta\dot{d}(t)$. Similarly, for the upper extreme, it is valid

$$\dot{d} - \dot{L} - a\omega\cos(\omega t) = \delta\dot{L}, \tag{35}$$

with

$$\int_0^\infty |\delta\dot{L}|dt = c_2 \tag{36}$$

and $c_2 > 0$ being another constant for a bounded response. In the same way, the upper extreme of the cable is then tensed conveniently by selecting the function $\delta\dot{L}(t)$. Thus, the energy deployed by the cable force controllers for damping down a spurious is finite.

However, since forces (28) and (30) are involved in the ROV dynamics, the ROV velocity controller can compensate these nonlinearities in order to accomplish high-quality performance, mainly in the nonconvex zone of (28).

Finally, measurement of F_c, L, and $\dot{d}$ is necessary for the implementation of the control law (27). Additionally, the motion of the crane jib, i.e., $a\sin(\omega t)$, must also be known, at least roughly. Another general requisite in the design is that the use of high derivatives in the control law design would be avoided as far as possible.

5.2 Design of a ROV velocity controller

In order to reach a high-quality control of the ROV kinematics, we focus the design of a reference controller with a tunable reference dynamics. A realizable control law is proposed which is able to force the ROV velocity $\dot{d}$ to track an auxiliary velocity $\dot{d}_m$, which is the output of a reference dynamics given by

$$\dot{d}_m = \frac{\beta_0}{\Lambda(s)}\dot{d}_{\text{ref}}, \tag{37}$$

where $\dot{d}_{\text{ref}}$ is a piecewise continuous and bounded reference signal of the control system, β_0 a gain, and $\Lambda(s)$ a Hurwitz polynomial, whose order will be determined next.

Denoting $\upsilon = u_{\text{t}}|u_{\text{t}}|$ as the auxiliary control action of the thrusters and taking (9), (10), and (30) into account, one gets a basic equation of the system dynamics for controller design

$$\begin{aligned}\upsilon = {} & \frac{m+m_\infty}{K_{\text{t}}}(s^2+\gamma_1 s+\gamma_0)\,\ddot{d} \\ & + \frac{\pi\rho D^2}{8K_{\text{t}}}(s^2+\gamma_1 s+\gamma_0)C_{\text{D}}(\dot{d})\dot{d}|\dot{d}| \\ & - (s^2+\gamma_1 s+\gamma_0)\frac{1}{K_{\text{t}}}F_{\text{c}} - \gamma_0\frac{m-\frac{\pi\rho D^3}{6}}{K_{\text{t}}}g.\end{aligned} \tag{38}$$

The last equation manifests a differential relation of third order with a high degree of nonlinearity between $\dot{d}$ and υ. So, the order of $\Lambda(s)$ has to be 3 in order for the reference dynamics to have a relative degree equal to the order of the system dynamics. Thus,

$$\Lambda(s) = s^3+\alpha_2 s^2+\alpha_1 s+\alpha_0, \tag{39}$$

where the coefficients of α_i determine the desired behavior of the reference dynamics.

In order to achieve the model-following objective (37) according to the structure in Fig. 28, a suitable control law must combine similar linear and nonlinear terms in (38) according to

$$\begin{aligned}\upsilon = {} & \frac{\theta_1}{\Lambda_f}\upsilon + \frac{\theta_2}{\Lambda_f}\dot{d} + \frac{\theta_3}{\Lambda_f}F_{\text{v}} + \frac{\theta_4}{\Lambda_f}F_{\text{c}} + \frac{\theta_5}{\Lambda_f}\ddot{d} \\ & + \frac{\theta_6}{\Lambda_f}\dot{F}_{\text{v}} + \frac{\theta_7}{\Lambda_f}\dot{F}_{\text{c}} + \frac{\theta_8}{\Lambda_f}\ddot{F}_{\text{v}} + \frac{\theta_9}{\Lambda_f}\ddot{F}_{\text{c}} + \theta_{10}\dot{d} \\ & + \theta_{11}F_{\text{v}} + \theta_{12}F_{\text{c}} + \theta_{13}\ddot{d} + \theta_{14}\dot{F}_{\text{v}} + \theta_{15}\dot{F}_{\text{c}} \\ & + \theta_{16}\ddot{F}_{\text{v}} + \theta_{17}\ddot{F}_{\text{c}} + \theta_{18} + \theta_{19}\dot{d}_{\text{ref}},\end{aligned} \tag{40}$$

where θ_i are the controller coefficients, $F_{\text{v}} = -C_{\text{D}}(\dot{d})\,\dot{d}|\dot{d}|$, and Λ_f is an adjustable Hurwitz polynomial, for instance, of the simple form

$$\Lambda_f = s + a_0, \tag{41}$$

whose minimal order helps to minimize the number of θ_i necessary to achieve the objective.

Hence, the control action is obtained through the inverse relation

$$u_{\text{t}} = \text{sign}(\upsilon)\sqrt{|\upsilon|}, \tag{42}$$

which is subject to saturation according to (30).

From (40) and using $\Lambda_f\dot{d}_{\text{ref}} = (\Lambda_f\Lambda\dot{d})/\beta_0$, one gets

$$\begin{aligned}(\Lambda_f-\theta_1)\upsilon = {} & \theta_2\dot{d} + \theta_3 F_{\text{v}} + \theta_4 F_{\text{c}} + \theta_5\ddot{d} + \theta_6\dot{F}_{\text{v}} \\ & + \theta_7\dot{F}_{\text{c}} + \theta_8\ddot{F}_{\text{v}} + \theta_9\ddot{F}_{\text{c}} + \theta_{10}\Lambda_f\dot{d} \\ & + \theta_{11}\Lambda_f F_{\text{v}} + \theta_{12}\Lambda_f F_{\text{c}} + \theta_{13}\Lambda_f\ddot{d} \\ & + \theta_{14}\Lambda_f\dot{F}_v + \theta_{15}\Lambda_f\dot{F}_{\text{c}} + \theta_{16}\Lambda_f\ddot{F}_{\text{v}} \\ & + \theta_{17}\Lambda_f\ddot{F}_{\text{c}} + \theta_{18}a_0 + \theta_{19}\Lambda_f\Lambda\,\dot{d}/\beta_0,\end{aligned} \tag{43}$$

and with (38) one achieves

$$\begin{aligned}(\Lambda_f-\theta_1)\upsilon = {} & \frac{m+m_\infty}{K_{\text{t}}}(\Lambda_f-\theta_1)(s^3+\gamma_1 s^2+\gamma_0 s)\,\dot{d} \\ & + \frac{\pi\rho D^2}{8K_{\text{t}}}(\Lambda_f-\theta_1)(s^2+\gamma_1 s+\gamma_0)F_{\text{v}} \\ & - (\Lambda_f-\theta_1)\left(\frac{1}{K_{\text{t}}}s^2+\frac{\gamma_1}{K_{\text{t}}}s+\frac{\gamma_0}{K_{\text{t}}}\right)F_{\text{c}} \\ & - \gamma_0\frac{m-\frac{\pi\rho D^3}{6}}{K_{\text{t}}}g(a_0-\theta_1).\end{aligned} \tag{44}$$

Equaling both the last expressions, one obtains a set of four equations to determine the controller coefficients of θ_i, namely:

(1) a relation associated with a polynomial in $\dot{d}$

$$\begin{bmatrix} \frac{m+m_\infty}{K_t} \\ \frac{m+m_\infty}{K_t}(\gamma_1+a_0) \\ \frac{m+m_\infty}{K_t}(\gamma_0+a_0\gamma_1) \\ \frac{m+m_\infty}{K_t}a_0\gamma_0 \\ 0 \end{bmatrix} = \begin{bmatrix} 0 & 0 & 0 & 0 & 0 & \frac{1}{\beta_0} \\ \frac{m+m_\infty}{K_t} & 0 & 0 & 0 & 0 & \frac{\alpha_2+a_0}{\beta_0} \\ \frac{(m+m_\infty)\gamma_1}{K_t} & 0 & 0 & 0 & 1 & \frac{\alpha_1+a_0\alpha_2}{\beta_0} \\ \frac{(m+m_\infty)\gamma_0}{K_t} & 0 & 1 & 1 & a_0 & \frac{\alpha_0+a_0\alpha_1}{\beta_0} \\ 0 & 1 & 0 & a_0 & 0 & \frac{a_0\alpha_0}{\beta_0} \end{bmatrix} \times \begin{bmatrix} \theta_1 \\ \theta_2 \\ \theta_5 \\ \theta_{10} \\ \theta_{13} \\ \theta_{19} \end{bmatrix}; \quad (45)$$

(2) a relation associated with a polynomial in F_v

$$\begin{bmatrix} \frac{\pi\rho D^2}{8K_t} \\ \frac{\pi\rho D^2}{8K_t}(\gamma_1+a_0) \\ \frac{\pi\rho D^2}{8K_t}(\gamma_0+a_0\gamma_1) \\ \frac{\pi\rho D^2}{8K_t}a_0\gamma_0 \end{bmatrix} = \begin{bmatrix} 0 & 0 & 0 & 0 & 0 & 0 & 1 \\ \frac{\pi\rho D^2}{8K_t} & 0 & 0 & 1 & 0 & 1 & a_0 \\ \frac{\pi\rho D^2}{8K_t}\gamma_1 & 0 & 1 & 0 & 1 & a_0 & 0 \\ \frac{\pi\rho D^2}{8K_t}\gamma_0 & 1 & 0 & 0 & a_0 & 0 & 0 \end{bmatrix} \times \begin{bmatrix} \theta_1 \\ \theta_3 \\ \theta_6 \\ \theta_8 \\ \theta_{11} \\ \theta_{14} \\ \theta_{16} \end{bmatrix}; \quad (46)$$

(3) a relation associated to a polynomial in F_c

$$\begin{bmatrix} -\frac{1}{K_t} \\ -\frac{(\gamma_1+a_0)}{K_t} \\ -\frac{\gamma_0+a_0\gamma_1}{K_t} \\ -\frac{a_0\gamma_0}{K_t} \end{bmatrix} = \begin{bmatrix} 0 & 0 & 0 & 0 & 0 & 0 & 1 \\ -\frac{1}{K_t} & 0 & 0 & 1 & 0 & 1 & a_0 \\ -\frac{\gamma_1}{K_t} & 0 & 1 & 0 & 1 & a_0 & 0 \\ -\frac{\gamma_0}{K_t} & 1 & 0 & 0 & a_0 & 0 & 0 \end{bmatrix} \begin{bmatrix} \theta_1 \\ \theta_4 \\ \theta_7 \\ \theta_9 \\ \theta_{12} \\ \theta_{15} \\ \theta_{17} \end{bmatrix}; \quad (47)$$

(4) a relation associated with the independent term

$$\left[-\gamma_0\frac{m-\frac{\pi\rho D^3}{6}}{K_t}ga_0\right] = \left[-\gamma_0\frac{m-\frac{\pi\rho D^3}{6}}{K_t}g\ a_0\right]\begin{bmatrix} \theta_1 \\ \theta_{18} \end{bmatrix}. \quad (48)$$

As seen in (45)–(48), there exist more unknowns than equations for the identification of the coefficients of θ_i. Equation (45) describes an overparametrized system with one free parameter and five unknown parameters. Similarly, (46) and (47) have three free parameters and four unknowns each, and (48) has one free parameter and one unknown. The problem now is to decide which coefficients would be free and which one would be unknown.

An analysis carried out in (45) reveals that either θ_1 or θ_{13} or θ_{19} should not be fixed, since the problem would become singular. However, choosing θ_2 or θ_5 or θ_{10}, the determination of the rest should be viable. As θ_1 is calculated by (45), then (46) and (47) will contain only two free parameters each. It is observed that θ_{16} and θ_{17} are irremovable in (46) and (47), respectively, and that the pairs $\{\theta_8, \theta_{14}\}$ and $\{\theta_{15}, \theta_9\}$ cannot be eliminated due to singularity.

However, only those parameters that are involved in terms with high derivatives are to be potentially eliminated. Under this criterion, for instance, θ_5, θ_6, θ_7, θ_8, and θ_9 can be eliminated. This, basically, leads to a minimal and optimal configuration of the controller coefficients.

Besides, there exists a last requirement of damping down transients when the controller starts from an equilibrium point at $t = 0$. For instance, this can be achieved by imposing $\upsilon(0) = 0$. From (40), it is seen that for all derivatives and filtered variables equal to zero at $t = 0$, another condition emerges between θ_{12} and θ_{18}, e.g.,

$$\begin{aligned}\upsilon(0) &= \theta_{12}\, F_{\mathrm{c}}(0) + \theta_{18} \\ &= 0\end{aligned} \tag{49}$$

So, from the set of redundant parameters $\{\theta_5, \theta_6, \theta_7, \theta_8, \theta_9\}$, one chooses the parameter that is able to accomplish minimal-set design and long-term transient elimination simultaneously. A glance at (40) reveals that θ_7 is the more suitable parameter because it involves a filtered first derivative of F_{c}, while the others are embedded in terms involving higher derivatives of variables. In this way, $\upsilon(0) = 0$.

Bearing in mind this reason, one concludes that the minimal-set selection yielding

$$\begin{aligned}\upsilon = {} & \frac{\theta_1}{\Lambda_f}\upsilon + \frac{\theta_2}{\Lambda_f}\dot{d} + \frac{\theta_3}{\Lambda_f}F_{\mathrm{v}} + \frac{\theta_4}{\Lambda_f}F_{\mathrm{c}} + \frac{\theta_7}{\Lambda_f}\dot{F}_{\mathrm{c}} \\ & + \theta_{10}\dot{d} + \theta_{11}\, F_{\mathrm{v}} + \theta_{12}F_{\mathrm{c}} + \theta_{13}\ddot{d} + \theta_{14}\,\dot{F}_{\mathrm{v}} + \theta_{15}\,\dot{F}_{\mathrm{c}} \\ & + \theta_{16}\,\ddot{F}_{\mathrm{v}} + \theta_{17}\,\ddot{F}_{\mathrm{c}} + \theta_{18} + \theta_{19}\dot{d}_{\mathrm{ref}}\end{aligned} \tag{50}$$

is quite suitable. Then, the control action results from (42), with (50) and saturations given in (30).

It is worth noticing that the employment of an observer is necessary to obtain high derivatives of $\dot{d}$, F_{v}, and F_{c}, since these are commonly not measurable. For this purpose, a nonlinear observer is described in [15].

5.3 Force controllers

The cable strength is controlled from the upper and lower extremes of the cable according to the structure proposed in Fig. 28. From (33), one sees that the lower extreme of the cable can be tensed by defining a perturbation $\delta\dot{d}(t)$ about the equilibrium point of the cable force defined by (32). Taking the nonlinearity (29) also into account, a PD controller will be able to generate $\delta\dot{d}$. However, its gain has to be variable to compensate the cable length changes. Thus,

$$\delta\dot{d}(t) = (d(t) + b)\big(K_{P_1} + K_{D_1}s\big)\big(F_{c_{\mathrm{ref}}} - F_{\mathrm{c}}\big). \tag{51}$$

Similarly, using (35) and (29) for the upper extreme of the cable, the crane motor will be perturbed by acting directly on its voltage by means of another PD controller, which generates

$$\delta\dot{L}(t) = (d(t) + b)\big(K_{P_2} + sK_{D_2}\big)\big(F_{c_{\mathrm{ref}}} - F_{\mathrm{c}}\big). \tag{52}$$

In both the cases, the PD controller parameters are set constant for a desired behavior of the cable tension. The tuning of these four coefficients is performed simultaneously by numerically optimizing a quadratic cost functional of the force error. To this end, the model reference (37) is employed directly instead of the cinematic control system described in the previous section, i.e., one assumes $\dot{d} = \dot{d}_m$. Moreover, the parameter tuning is performed for a monochromatic perturbation of the wave with amplitude $a = 1$ m and frequency $\omega = 0.55$ rad/s. The well-known robustness of the PD controllers is taken as an argument to achieve a good control performance for other settings of the wave in the real control system.

Finally, a fixed PD controller is applied for the hoisting crane (see Fig. 28) with equation

$$u_{\mathrm{cr}}(t) = \big(K_{P_3} + sK_{D_3}\big)(L_{\mathrm{ref}} - L). \tag{53}$$

The controller coefficients are tuned in the control loop of the hoisting system separately from the control loop of the umbilical–ROV system. For this purpose, the model in (31) with saturations is taken into account.

5.4 Summary of control components

The components of the controlled umbilical–ROV system are summarized in Table 3.

In order to simulate the controlled umbilical–ROV system in a wide range of heave operations, the controllers and actuators are selected with design parameters given according to Table 4. Other settings are indicated in the figures that illustrate the results.

The dynamic model used in the numerical simulations is model 2.

6 Control stability

The taut–slack control system described in the previous section is simulated and its steady-state dynamics are compared with the uncontrolled dynamics for identical

Table 3 Control system components

Control components	Input (s)	Output (s)	Equation
Umbilical–ROV	$\begin{cases} L \\ u_{\mathrm{t}} \end{cases}$	$\begin{cases} F_{\mathrm{c}} \\ \dot{d} \end{cases}$	$\begin{cases} (4), (5) \\ (9), (10) \\ (17), (18) \end{cases}$
Propulsion system	u_{t}	F_{t}	(30)
Crane	u_{cr}	L	(31)
Cinematic controller	$\begin{cases} \dot{d}_{\mathrm{ref}} \\ \dot{d} \\ F_{\mathrm{c}} \end{cases}$	u_{t}	(42), (50)
Reference model	$\dot{d}_{\mathrm{ref}}$	$\dot{d}_m$	(37), (39)
Force controller 1	$F_{c_{\mathrm{ref}}} - F_{\mathrm{c}}$	$\delta\dot{L}$	(52)
Force controller 2	$F_{c_{\mathrm{ref}}} - F_{\mathrm{c}}$	$\delta\dot{d}$	(51)
Crane controller	$L_{\mathrm{ref}} - L$	u_{cr}	(53)

Table 4 Parameter settings for simulations

System component	Coefficient set	Values in S.I. units
Reference model	$\{K_m, \alpha_2, \alpha_1, \alpha_0\}$	$\{6.498, 4.80, 9.01, 6.498\}$
Kinematic controller	$\{\theta_1, \theta_2, \theta_3, \theta_4, \theta_7, \theta_{10}, \theta_{11}, \theta_{12}, \theta_{13}, \theta_{14}, \theta_{15}, \theta_{16}, \theta_{17}, \theta_{18}, \theta_{19}\}$	$\{-3.80, -767.78, 359.89, -1.96 \times 10^{-13}, 0.89, 111.32, 94.70, -1.12, -708.17, 227.30, -0.56, 47.35, -0.11, -594.42, 656.45\}$
Hoisting crane motor	$\left\{k_1, \frac{L_a J}{k_1 k_2}, \frac{R_a J}{k_1 k_2}\right\}$	$\{0.015, 0, 5\}$
Force controller 1	$\{K_{P_1}, K_{D_1}\}$	$\{0.0016, 4.5 \times 10^{-14}\}$
Force controller 2	$\{K_{P_2}, K_{D_2}\}$	$\{0.0021, 0.0034\}$
Crane controller	$\{K_{P_3}, K_{D_3}\}$	$\{1700.0, 1320.0\}$
Propulsion system	$\{K_{\mathrm{t}}, \gamma_1, \gamma_0\}$	$\{8.5, 1, 2\}$
Thruster voltage saturation	$\{u_{\mathrm{t\,min}}, u_{\mathrm{t\,min}}\}$	$\{-12, 12\}$
Crane voltage saturation	$\{u_{\mathrm{cr\,min}}, u_{\mathrm{cr\,min}}\}$	$\{-110, 110\}$
Umbilical cable	$\{EA_0, b\}$	$\{10^6, 3\}$
ROV dynamics	$\{D, m\}$	$\{1, 590.36\}$
Hydrodynamics	$\{m_\infty, \rho, C_{\mathrm{D}}(Re)\}$	$\{268.35, 1025,$ Equation (7)$\}$

values of their common parameters. As given in Section 4, most of these parameters are suitable for a bifurcation study and to establish stability regions free of the taut–slack phenomenon. Similarly, here, the parametric space for determining stability regions is defined as

$$\mu = [a, \quad \omega, \quad D, \quad EA_0, \quad L]^{\mathrm{T}}, \tag{54}$$

where F_{t} is not longer available as free parameter, since it is regulated by the ROV cinematic and force controllers.

The detection of high periods is carried out in the same way as done in Section 3. Similarly as shown earlier, the zone drawn in shades corresponds to regions where the cable remains taut, at least in steady state, for a monochromatic perturbation.

Figure 29 depicts the qualitative diversity of behavior that can be produced in the heave operation under the control system with respect to the wave amplitude. In this sense, it is noticed that the variety of periodic solutions has been increased inside and decreased outside the stability region in comparison with homologous case without control. Additionally, one observes that the control imposes a tendency to chaos, however, with damped energy. A significant increment of the stable region L versus a is observed. One important property of the results shown in Section 3 is that the stability region is exclusively represented by period-1 solutions. Now in the controlled case, the appearance of high-period orbits and even chaos are common.

Figure 30 shows also a significative extension of the stability region d versus ω with the same characteristic as before. The tendency to chaotic behaviors is found out inside and outside the stability region mainly for small and middle cable lengths.

Figure 31 illustrates the stability in the region a versus ω at a mean depth. The increment of the stability

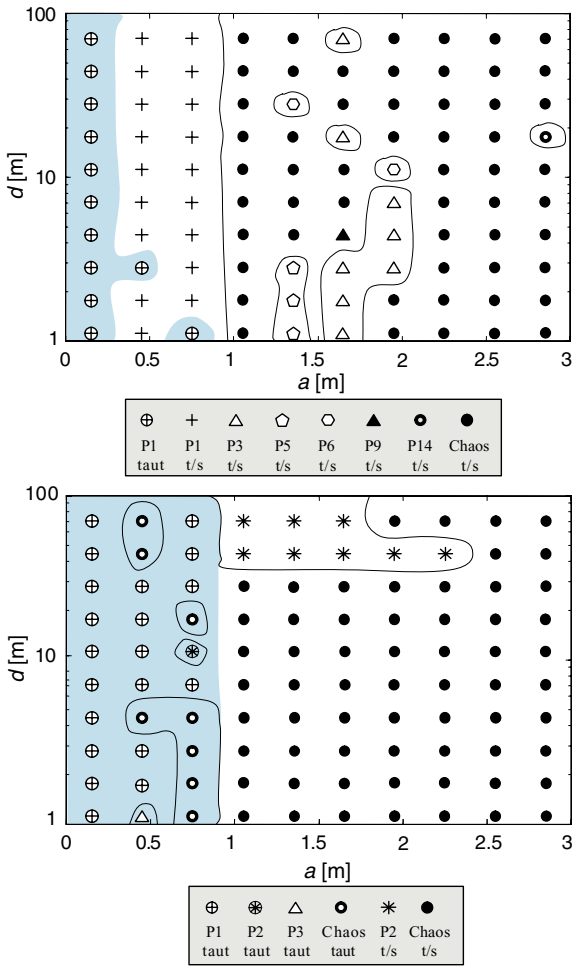

Fig. 29 Comparison of stability regions: ROV depth vs. wave amplitude for $EA_0 = 10^6$ N and $\omega = 1$ rad/s. (*Top*) Without control. (*Bottom*) With control

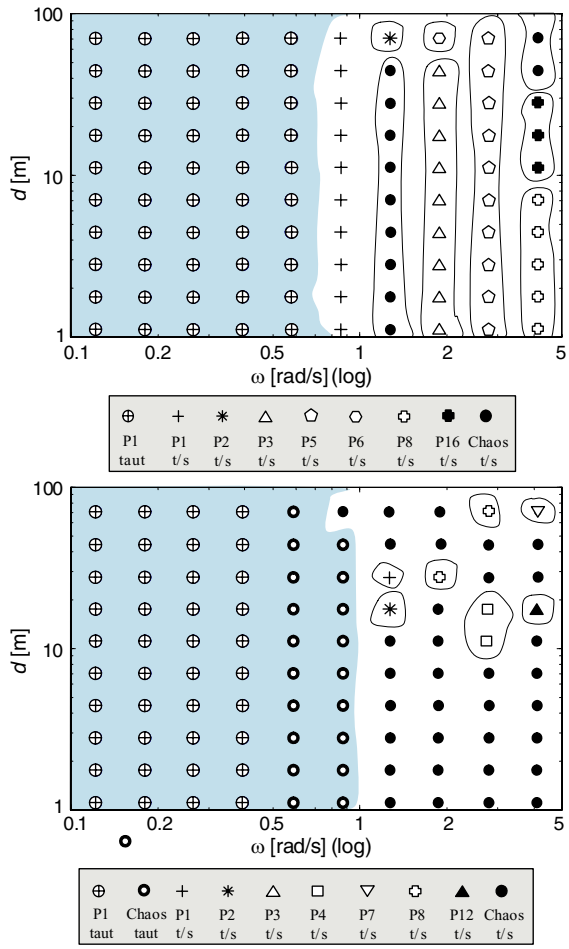

Fig. 30 Comparison of stability regions: ROV depth vs. wave frequency for $EA_0 = 10^6$ N and $a = 1$ m. (*Top*) Without control. (*Bottom*) With control

region is registered mainly for small wave amplitudes and large frequencies. The reason for the control not being so effective is pointed out in the previous section about the limited energy of the thrusters and crane motor, which are able to cope with a restrained wave steepness (ωa). The behavior diversity has not changed too much comparatively inside the stability region.

Figure 32 shows the region D versus EA_0 for a given wave and depth. It reflects the dependence between ROV weight and volume, and cable stiffness. Also, in this case, it was possible to obtain an extension of the stability region. It is inferred that a great volume with a relatively small cable stiffness is easy to control than is otherwise possible.

The appearance of chaotic behaviors is very common in the controlled case even in the stability region. One strange attractor is depicted in Fig. 33 with a cross section of its volume for $\ddot{d} = -10\,\mathrm{m/s^2}$. The attractor shape is very common for other points considered in the study.

7 Control performance

In this section, an investigation of the overall control performance of the system in the sinking/lifting operation is presented. The first experiments consist of prescribing a profile of the desired depth to be followed in the shortest possible time, explaining the maximal

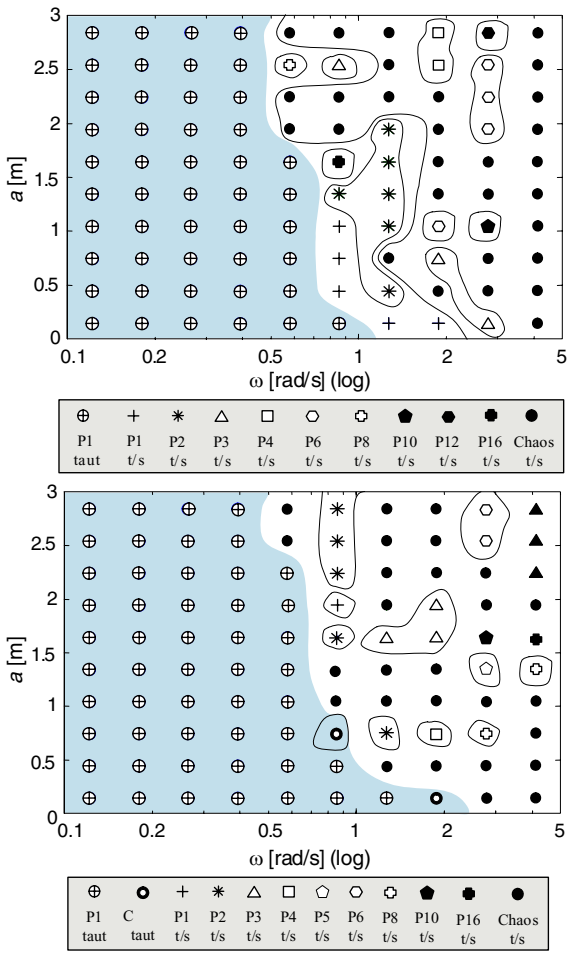

Fig. 31 Comparison of stability regions: Wave amplitude vs. wave frequency for $L = 50\,\text{m}$ and $EA_0 = 10^6\,\text{N}$. (*Top*) Without control. (*Bottom*) With control

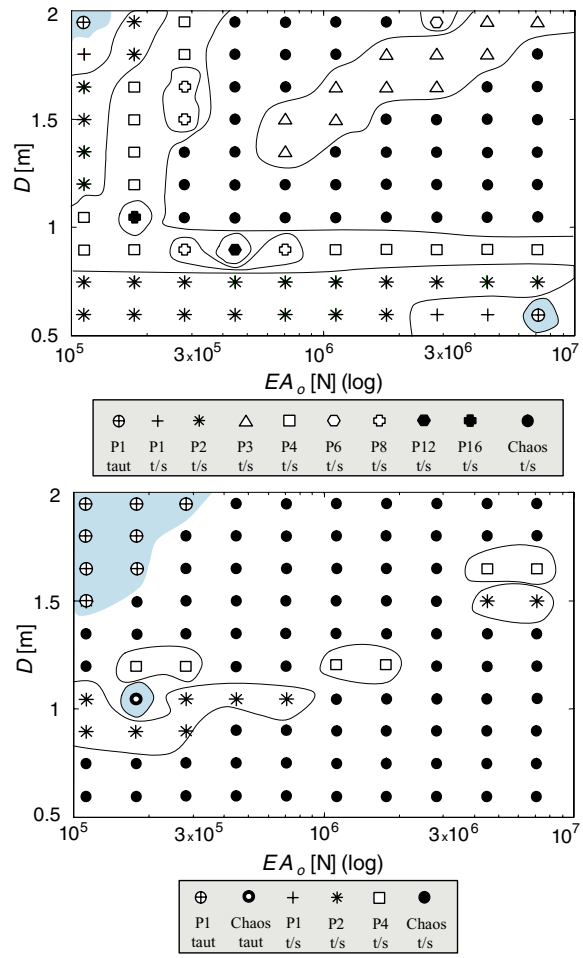

Fig. 32 Comparison of stability regions: ROV diameter vs. stiffness constant for $L = 50\,\text{m}$, $\omega = 1\,\text{rad/s}$, and $a = 1\,\text{m}$. (*Top*) Without control. (*Bottom*) With control

cable strength and avoiding the entry into the taut–slack region as far as possible.

In Figs. 34–37, the profiles of the reference L_{ref} are the same and are built up as ramps for sinking up to 100 m from a starting depth $L = 15\,\text{m}$ (i.e., $d = 12\,\text{m}$), pausing and lifting again to the same depth as in the beginning. The dynamics are subject to different perturbations explained in the next.

In Fig. 34, the wave steepness amounts to $(a\omega) = 0.275\,\text{m rad/s}$. The cable force is regulated about the value $F_{\text{ref}} = 526\,\text{N}$. It is seen that the force controllers are able to maintain the oscillations that are quite small about this reference point. The cable tension fluctuates mainly about singular points of the profile, i.e., when $\dot{L}(t)$ is discontinuous, otherwise it behaves smoothly. The ROV velocity $\dot{d}$ is underdamped during the changes. Notice that $\dot{d}$ has a similar path as the reference velocity $\dot{d}_{\text{ref}}$, except during a short period with high-frequency oscillations caused by transients of the equivalent mass–spring system. Figure 35 shows the evolution of the control actions on the ROV thrusters and crane motor, respectively. The first one shows an increment of the energy of u_{t} with even a saturation for a short time. On the other side, the control action for the crane motor shows a continuous oscillatory behavior with steps at the break points of L_{ref}. The frequency of these oscillations correspond to the wave frequency, indicating that during the sinking/lifting of the ROV, the crane motor attempts to follow the wave perturbation in order to care for the cable strength and simultaneously

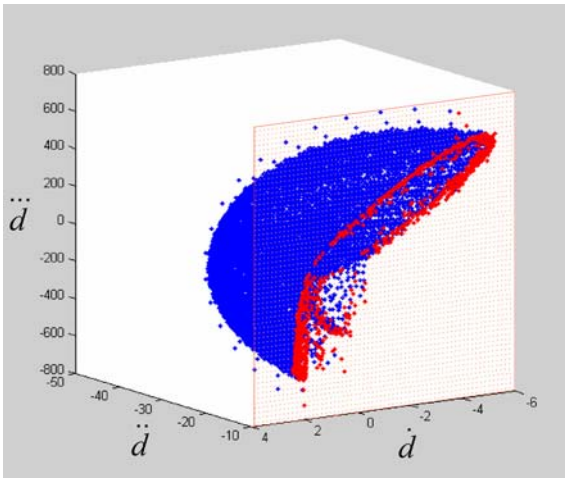

Fig. 33 Construction of a strange attractor for the control system behavior with $a = 0.45\,\text{m}$, $\omega = 4.11\,\text{rad/s}$, $EA_0 = 10^6$, and $L = 50\,\text{m}$. Cross section for $\ddot{d} = -10\,\text{m/s}^2$

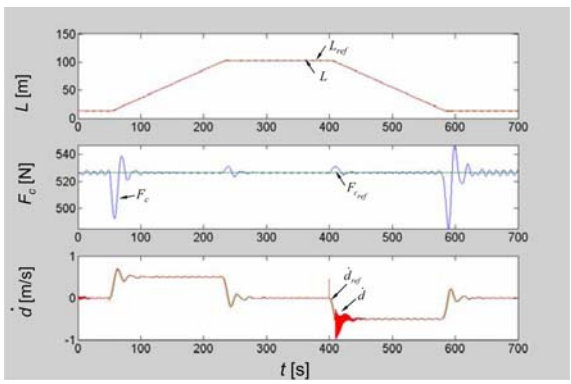

Fig. 34 Evolution of the ROV cable length, cable force, and ROV velocity for $a = 0.5\,\text{m}$, $\omega = 0.55\,\text{rad/s}$, and $EA_0 = 10^6\,\text{N}$

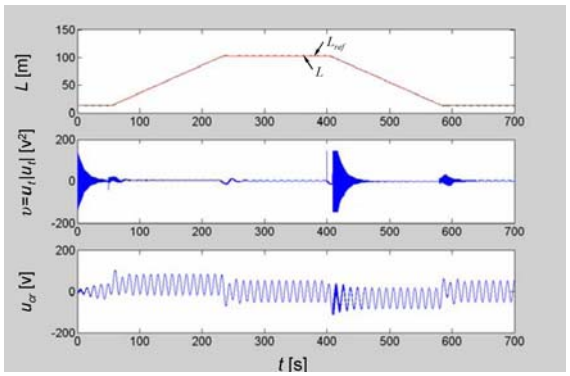

Fig. 35 Evolution of the cable length, square tension of the thrusters, and tension of the crane motor for $a = 0.5\,\text{m}$, $\omega = 0.55\,\text{rad/s}$, and $EA_0 = 10^6\,\text{N}$

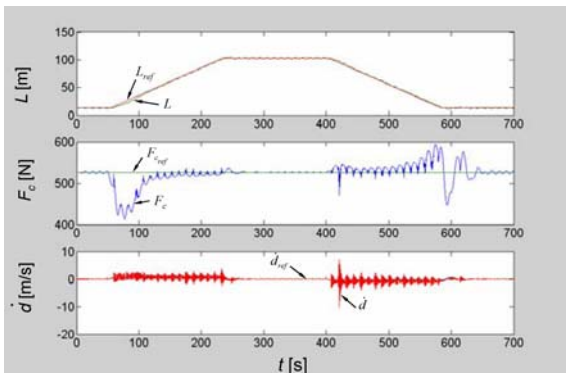

Fig. 36 Evolution of the cable length, cable force, and ROV velocity for $a = 0.75\,\text{m}$, $\omega = 0.55\,\text{rad/s}$, and $EA_0 = 10^6\,\text{N}$

diminish the error $(d_{\text{ref}} - d)$. In summary, the overall achievable performance in this operation is of high quality.

The next experiment, illustrated in Figs. 36 and 37, exemplifies the control behavior under a larger wave steepness than in the previous case. It amounts $(a\omega) = 0.4125\,\text{m rad/s}$. The cable force is regulated as before about the value $F_{\text{ref}} = 526\,\text{N}$. In this case, the oscillation of the force in the transient phase is stronger than in the earlier case but less than 20% of the reference value. The ROV velocity $\dot{d}$ behaves more irregular than in the former case, but the overall performance of the operation is nevertheless very good. The evolution of the thruster excitation v saturates during the ascent and descent, and turns off in the pause. However, the control action for the crane motor saturates from time to time, sometimes recovering the low-frequency oscillation with a wave-shaped appearance. The error $(L_{\text{ref}} - L)$ is mainly perceived in the starting phase, after an ascent or descent; however, it amounts a maximal value less than 5% of the total change of the length.

The next couple of Figs. 38–41 show the control performance for the regulation operation about a fixed depth $d_{\text{ref}} = L_{\text{ref}} - b = 47\,\text{m}$ under wave perturbations.

In the first case, the control variables L, F_c, and $\dot{d}$ show relatively small variations along the time for a wave steepness $(a\omega) = 0.387\,\text{m rad/s}$. Also, here, the effect of the wave perturbation can be seen in the steady-state oscillation. The control action for the thrusters has a fundamental component in the wave frequency and a small high-frequency oscillation produced by the elongation of the cable. This effect does

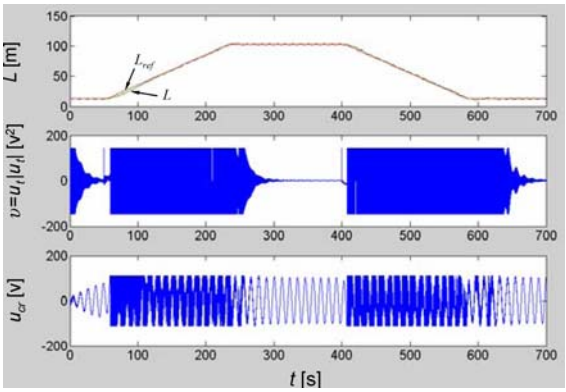

Fig. 37 Evolution of the cable length, square tension of the thrusters, and tension of the crane motor for $a = 0.75$ m, $\omega = 0.55$ rad/s, and $EA_0 = 10^6$ N

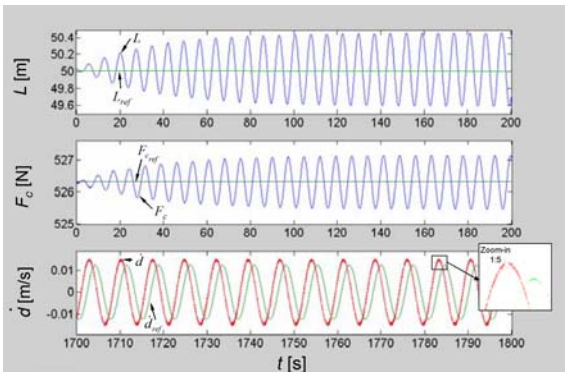

Fig. 38 Evolution of the cable length, cable force, and ROV velocity for a wave amplitude $a = 0.45$ m, frequency $\omega = 0.86$ rad/s, and $EA_0 = 10^6$ N

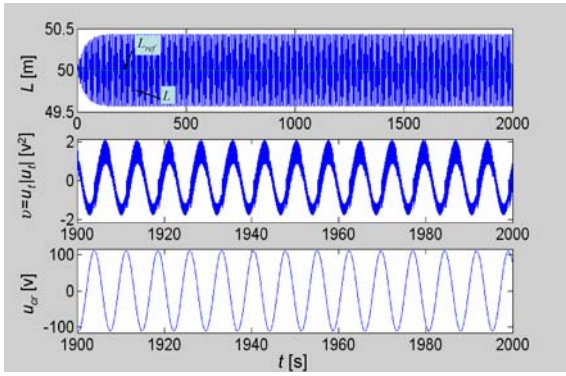

Fig. 39 Evolution of the cable, length, square tension of the thrusters, and tension crane motor for a wave amplitude $a = 0.45$ m, frequency $\omega = 0.86$ rad/s, and $EA_0 = 10^6$ N

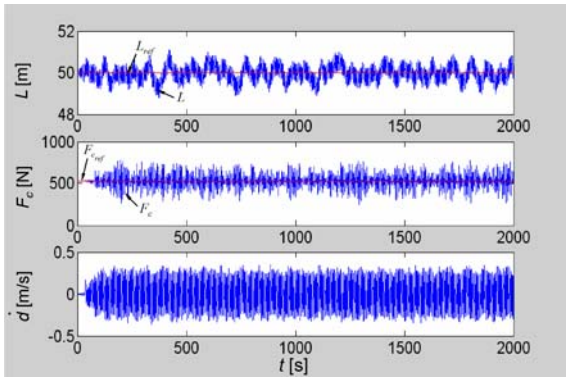

Fig. 40 Evolution of the cable length, cable force, and ROV velocity for a wave amplitude $a = 0.75$ m, frequency $\omega = 0.86$ rad/s, and $EA_0 = 10^6$ N

not appear by the control action for the crane motor, whose behavior is sine-shaped.

Figures 40 and 41 depict the control performance for a significative larger wave steepness ($a\omega$) than the case before, equal to 0.645 m rad/s. In this case, the behavior becomes chaotic for all variables; however, the control goal of maintaining the cable tense is achieved. Despite the almost permanent saturation of the control action for the thrusters, the depth and length errors are less than 2% of the reference values and the taut–slack phenomenon is quite afar.

8 Cable tension

The presence of the taut–slack phenomenon during the sinking/lifting operation of the ROV demands a significant stress resistance from the umbilical cable. The rampant rising and large strengths may not only be the cause of premature fatigue but also of overcoming the cut resistance of the cable. In this section, the cable tension is analyzed in qualitatively different stationary behaviors of the ROV operation. To this end, some selected scenarios of the Figs. 29–32 are picked up and their corresponding comparative force evolution is depicted. The comparison involves the uncontrolled and the controlled systems in a common figure.

Figure 42 reproduces the evolution of the forces for a relatively small wave steepness equal to 0.28 m rad/s. After a transient period, the uncontrolled system enters the taut–slack zone with evidence of hefty hauls of the cable. In contrast, the controlled system can successfully regulate the force about the reference in the taut zone.

The next four figures illustrate the force evolution for a relatively large wave amplitude equal to 0.75 m and high frequencies, ranging from 0.86 to 1.27 rad/s,

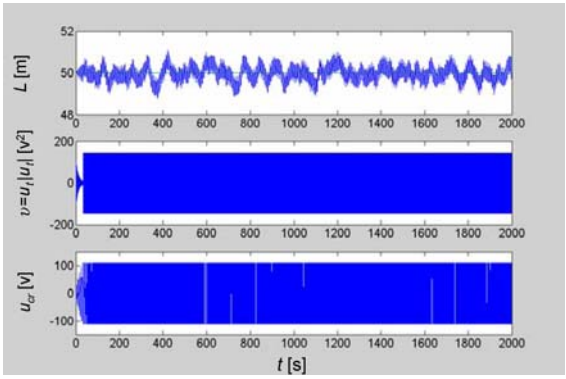

Fig. 41 Evolution of the cable, length, square tension of the thrusters, and tension crane motor for a wave amplitude $a = 0.75$ m, frequency $\omega = 0.86$ rad/s, and $EA_0 = 10^6$ N

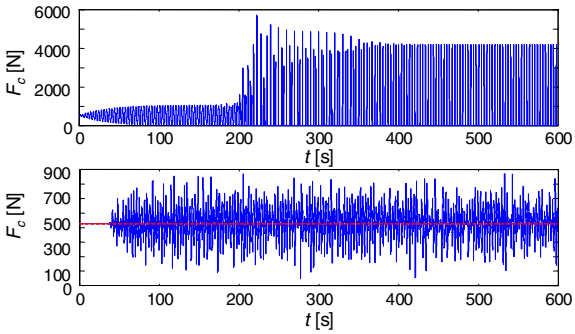

Fig. 42 Cable force comparison for $a = 0.15$ m, $\omega = 1, 87$ rad/s, and $L = 50$ m. (*Top*) Without control. (*Bottom*) with control

and lengths in the span starting at $L = 4.12$ up to 50 m. Figure 43 represents the force progressing under a wave steepness of $(a\omega) = 0.645$ m rad/s. Similarly as before, in the control system, the cable remains tense and the force regulated within a relatively narrow band, while the uncontrolled dynamics of the system produces large and stark increments of the tension circa 10 times larger than in the controlled case. Figures 44 and 45 characterize a similar situation for an increment of the wave steepness to $(a\omega) = 0.75$ m rad/s and two different lengths. Notice that the control of the cable tension becomes more difficult with increasing lengths; however, despite the increment in the error energy, the tension remains within a band without the appearance of the taut–slack phenomenon. Figure 46 shows the wave steepness $(a\omega) = 0.9527$ m rad/s. This seems to be too large with respect to energy available in the actuators to achieve the control goal. Thus, the taut–slack phenomenon cannot be avoided in the uncontrolled system as well. Additionally, one notices

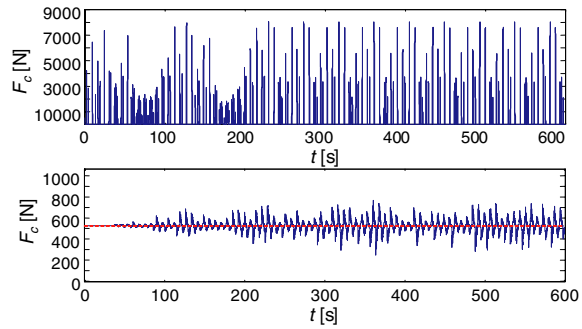

Fig. 43 Cable force comparison for $a = 0.75$ m, $\omega = 0$, 86 rad/s, and $L = 50$ m. (*Top*) Without control. (*Bottom*) With control

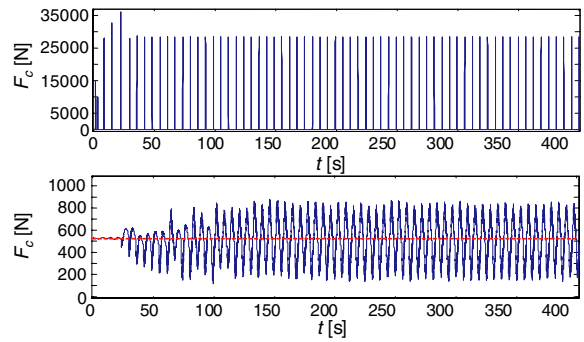

Fig. 44 Cable force comparison for $a = 0.75$ m, $\omega = 1$ rad/s, and $L = 4.12$ m. (*Top*) Without control. (*Bottom*) With control

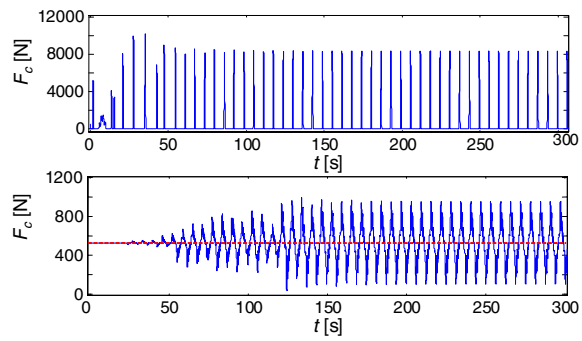

Fig. 45 Cable force comparison for $a = 0.75$ m, $\omega = 1$ rad/s, and $L = 47$, 66 m. (*Top*) Without control. (*Bottom*) With control

much more hefty oscillations in the controlled case than in the uncontrolled case.

The next three figures, Figs. 47–49, illustrate the force evolution for a greater wave amplitude than in the previous cases but with smaller wave frequencies. The wave energy remains constant in all the cases. They exemplify the same experiments as earlier but with three different lengths of $L = 14.22$, 47.66, and 73.80 m. In these runs, the control system can regulate the force

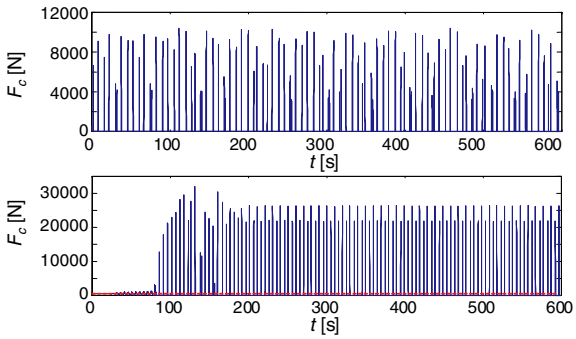

Fig. 46 Cable force comparison for $a = 0.75$ m, $\omega = 1.27$ rad/s, and $L = 50$ m. (*Top*) Without control. (*Bottom*) With control

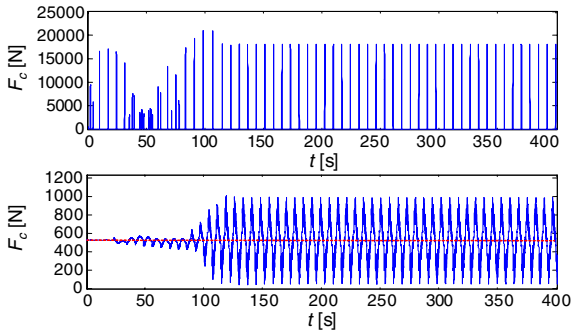

Fig. 47 Cable force comparison for $a = 1$ m, $\omega = 0.85$ rad/s, and $L = 14.22$ m. (*Top*) Without control. (*Bottom*) With control

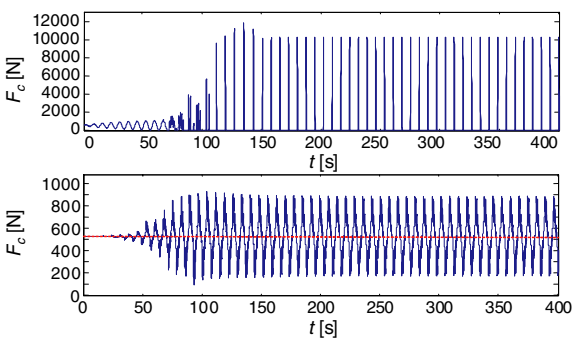

Fig. 48 Cable force comparison for $a = 1$ m, $\omega = 0.85$ rad/s, and $L = 47.66$ m. (*Top*) Without control. (*Bottom*) With control

satisfactorily; however, one notices that by increasing of the length, the limit for cable slackness will be closer.

Figure 50 displays an extreme situation where the wave steepness amounts a relatively large value of $(a\omega) = 0.903$ m rad/s for a middle length. Here, the control system works successfully; however, the operation stays within the limit of the cable slackness.

Summarizing, in the majority of the experiments, the control system had success in reaching the control goals. In contrast with the operation of the free system,

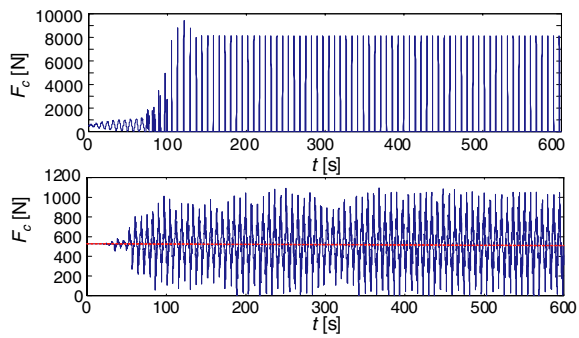

Fig. 49 Cable force comparison for $a = 1$ m, $\omega = 0.85$ rad/s, and $L = 73.80$ m. (*Top*) Without control. (*Bottom*) With control

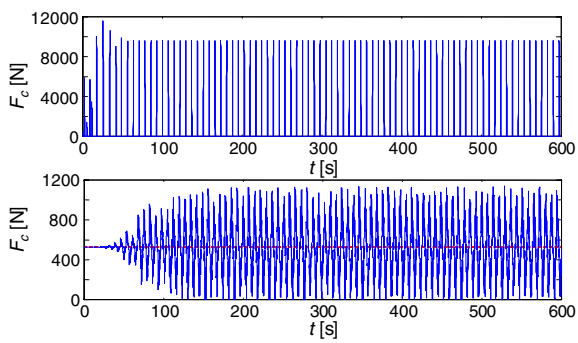

Fig. 50 Cable force comparison for $a = 1.05$ m, $\omega = 0, 86$ rad/s, and $L = 50$ m. (*Top*) Without control. (*Bottom*) With control

whose dynamics enters usually the taut–slack zone producing violent hauls of the cable, the control system can accomplish length path-following and regulation quite satisfactory with bounded cable force.

9 Conclusions

In this paper, the stability of an umbilical–ROV system under nonlinear oscillations in heave motion was analyzed using numerical methods for the uncontrolled and controlled cases comparatively. The focus is mainly on the appearance of the taut–slack phenomenon on the umbilical cable produced by the interaction of monochromatic waves with the ROV. Nonlinear elements were considered in the dynamics in three models with different degrees of physical knowledge. These encompass nonlinear drag damping, bilinear restoring force, radiation potential forces, and saturation of the actuators. It is concluded that the most complex model including all nonlinear elements produces the widest qualitatively diverse behavior in steady state,

even when the integration of radiation forces only contributes with improvements at superficial depths. In order to simplify the analysis, a ROV with spherical shape was selected and a nonlinear drag characteristic for this shape was introduced in the model. This characteristic varies with the Reynolds number and presents a nonconvex zone just in the span of the operating ROV velocities.

The sinking/lifting operation in a wide interval of the cable length is characterized by the appearance of the taut–slack phenomenon, which is described by hefty hauls of the cable with tension magnitudes close to the tolerable limits. This unpredictable behavior was observed in simulations of the uncontrolled ROV dynamics, mainly for significant wave steepness and great depths of operation. In the paper, a solution via control to avoid this phenomenon and in consequence its negative effects on the cable strength. The control system design is based on the composition of two criteria. First, the cable strength is regulated about a desired secure tension by pulling the extremes of the cable by means of the crane motor and ROV thrusters interactively and independently of the sinking/lifting profile. The second criterion is to design a velocity controller for the ROV that can compensate the nonlinearities of the drag coefficients and restoring force. This was achieved by means of a reference-model controller that specifies the desired reference behavior by means of a dynamic model of third order. The features of diverse operations in steady state by means of the controlled system and the free system are comparatively investigated under equal perturbations and parameter settings.

The comparative stability study is performed using physical bifurcation parameters and detection methods of high periods based on Poincaré maps and analysis of Cauchy series. The bifurcation parameters are divided into two sets, namely operation parameters (cable length, wave amplitude and frequency, thruster force) and design parameters (ROV shape, mass, and cable stiffness). One of the main results is the construction of stability regions that are free of these phenomenon on the free parameter space. They indicate a qualitative diversity in the behavior and possible routes to chaos from the stability regions to outside.

From the results, it was clear that stability regions can be extended considerably with the use of control, e.g., the control system can avoid the slackness of the cable in a heave operation despite the presence of wave perturbations. A uniqueness of the system is that stability regions can exhibit not only period-1 behaviors but also chaotic dynamics. The reason for this is the dominance of the restoring force of the cable against the hydrodynamic drag force. The limits between the taut and taut–slack zones are significantly influenced by the wave steepness, whose square value represents the energy of the perturbation. From a practical point of view, the effectiveness of the control system proposed here begins to fall off when the energy of the actuators is not sufficient to counteract the amount of the energy of the perturbation.

Future work is dedicated to the analysis of the phenomenon "taut–slack" in 3 degree of freedom in the operation of ROVs in estuaries, where the umbilical cable exerts harmonic tugs due to combined effects of steep waves with strong currents. The study of this dynamics is important in the design of vision control systems in order for the vehicle to maintain specified courses with constant attitude and pitch angle. Afterwards, this analysis will be complemented with experimental research in flow canal.

Acknowledgements The authors thank Prof. Dr.-Ing. Edwin Kreuzer and Dr.-Ing. Volker Schlegel at the Technical University of Hamburg-Harburg for the theoretical support. Also it is thanked the National Council for Science and Technology, Argentine, Universidad Nacional del Sur and Scientific Cooperation Project with Germany (AL/A99-EX II/17) for the financial support of this investigation.

References

1. AQWA: AQWA Reference Manual, Version 5.3A. Century Dynamics Ltd., UK (2002)
2. Behbahani-Nejad, M., Perkins, N.C.: Hydrodynamic and geometric stiffening effects on the out-of-plane waves of submerged cables. Nonlinear Dyn. **13**(3), 243–257 (1997)
3. Dmitrieva, I., Lougovsky, V.: Non-linear harmonic, subharmonic and chaotic motion of offshore structures. In: Proceedings of the 8th International Conference on the Behaviour of Offshore Structures, Vol. 2, pp. 205–218, Delft, The Netherlands (1997)
4. Feng, Z., Allen, R.: Evaluation of the effects of the communication cable on the dynamics of an underwater flight vehicle. Ocean Eng. **31**, 1019–1035 (2003)
5. Guckenheimer, J., Holmes, P.: Nonlinear Oscillations, Dynamical Systems and Bifurcations of Vector Fields. Springer-Verlag, Berlin (1997)
6. El-Hawary, F.: The Ocean Engineering Handbook. CRC Press, Boca Raton, FL (2001)
7. Ellermann, K., Kreuzer, E., Markiewicz, M.: Nonlinear dynamics of floating cranes. Nonlinear Dyn. **27**(2), 107–183 (2002)

8. Fossen, T.I.: Guidance and Control of Ocean Vehicles. Wiley, Chichester, UK (1994)
9. Huang, S.: Stability analysis of the heave motion of marine cable-body systems. Ocean Eng. **26**, 531–546 (1999)
10. Huang, S., Vassalos, D.: Heave response of a thetered subsea unit during the lunch and recovery process. In: Proceedings of the 2nd International Offshore and Polar Engineering Conference, San Francisco, CA (1992)
11. Indiveri, G.: Modelling and Identification of Underwater Robotic Systems, Ph.D. University of Genova (1998)
12. Jordán, M.A.: On-line identification and convergence analysis of excitation-force and drag-force models for moored floating structures. Ocean Eng. **33**, 1161–1213 (2006)
13. Jordán, M.A., Beltrán-Aguedo, R.: Nonlinear identification of mooring lines in dynamic operation of floating structures. Ocean Eng. **31**, 455–482 (2004)
14. Jordán, M.A., Beltrán-Aguedo, R.: Optimal identification of potential-radiation hydrodynamics for moored floating structures: A new general approach in state space. Ocean Eng. **31**, 1859–1914 (2004)
15. Jordán, M.A., Bustamante, J.L.: Diseño de un observador no-lineal para Robots subacuáticos en operación de ascenso/descenso. In: Proceedings of the III Jornadas Argentinas de Robótica, San Juan, June 3–4 (2004)
16. Kijima, K., Fossen, T.I. (eds.): Control Applications in Marine Systems. Pergamon Press, UK (2000)
17. Kleczka, W., Kreuzer, E.: On the systematic analytic-numeric bifurcation analysis. Nonlinear Dyn. **7**, 149–163 (1995)
18. Papazoglou, V.J., Mavrakos, A., Triantaffilou, M.S.: Nonlinear cable response and model testing in water. J. Sound Vib. **140**(1), 103–115 (1990)
19. Plaut, R.H., Farmer, A.L., Holland, M.M.: Bouncing-ball model of 'dry' motions of a tethered buoy. J. Vib. Acoustics **123**(3), 333–339 (2001)
20. Rosenwasser, E.N.: Oscillations of Non-Linear Systems. Nauka, Moscow (1969)
21. Smith, R.J: Taut–slack dynamics of a vertically suspended subsea unit. In: Proceedings of the International Conference on Offshore Mechanics and Arctic Engineering (OMAE), Vol. 1, pp. 873–884 (2001)